Quantifying sediment exhaustion of the Sattelkar cirque, Hohe Tauern, Austria

Master's Thesis

to achieve the
Master's degree MSc

at the Faculty of Natural and Life Sciences
of the Paris-Lodron-University Salzburg

Submitted by

Ricarda Elena Fink

Supervisor

Assoz.-Prof. Dr. Jan-Christoph Otto

Department of Environment and Biodiversity

Salzburg, April 2024

Abstract

High mountain landscapes are dynamic and heterogeneous environments shaped by diverse geomorphological processes, serving as primary sources of sediment and water with significant implications for downstream areas. This study investigates sediment dynamics within the Sattelkar cirque in the Hohe Tauern mountain range, Austria, which has experienced significant landslide activity since 2003. This research employs bedrock interpolation, multi-temporal digital elevation model (DEM) analysis and trend extrapolation from 2012-2023 to investigate sediment availability and exhaustion within the active landslide area as well as sediment dynamics of the landslide and corresponding debris cone. The analysis reveals significant variability in sediment volume across different sliding scenarios reaching approximately 1,000,000-1,800,000 m³. Observations indicate an increasing sediment discharge from the sliding area and accumulation in the debris cone. Estimations suggest a timeframe for sediment exhaustion between 2033 and 2042. Uncertainties in sediment volume quantification and extrapolation reliability emphasize the need for further research to enhance hazard assessment. While generalization is limited by the complexity of landslides, the findings contribute valuable insights into sediment dynamics within active landslides, fill gaps in existing data and provide information for future research efforts.

Acknowledgements

I would like to take this opportunity to express my gratitude to all those who have supported and motivated me throughout the completion of this Master's thesis. Naming all of these people would go beyond the scope. My special thanks therefore belong to the following people:

Firstly, I am deeply grateful to Assoz.-Prof. Dr. Jan-Christoph Otto not only for his excellent supervision despite his sabbatical but also for all his support and for enabling me to gain insights into a wide range of research topics throughout my studies. As a result, I was able to develop not only professionally but also personally and gain valuable experience.

I would particularly like to thank Dr. Markus Keuschnig and Robert Delleske of GEORESEARCH Forschungsgesellschaft mbH for enabling me to work on this interesting topic by providing the data, for taking me along for data acquisition and for enlightening discussions.

I would also like to thank Univ.-Prof. Dr. Andreas Lang, whose expertise and patient advice on the data quality treatment was extremely valuable.

Special appreciation goes to my partner, Michel Kahre, as well as to Sabine Dietel and Fabian Dremel, who constantly reorganised my thoughts, were always supportive and gave me advice.

Table of Contents

List of figures

List of tables

1 Introduction

Cirques usually represent glacially formed overdeepenings in high alpine areas (Evans and Cox 1974; Stroeven et al. 2013), thus enabling a recent influence by glaciers and permafrost (Keuschnig et al. 2021). An increase in pore water pressure due to permafrost degradation, snowmelt or heavy precipitation may facilitate the mobilisation of loose material in the form of mass movements such as landslides or debris flows and may therefore cause threat to humans and infrastructure (Damm and Felderer 2013; Gariano and Guzzetti 2016; Savi et al. 2021; Zhang et al. 2021). An almost doubling of heavy precipitation compared to 1921 and an increase in debris flows in the northern Limestone Alps (Dietrich and Krautblatter 2017) emphasize the relevance of studying sediment dynamics in high-alpine environments. In the future, further reductions in permafrost as well as changes in precipitation, snow cover duration and thickness and soil moisture will result from a comparatively strong increase in temperature in the Alpine region (Olefs et al. 2021; Vorkauf et al. 2021).

The Sattelkar cirque, located in the Hohe Tauern mountain range, Austria, has been experiencing landslide activity since 2003, whereby a progressively larger area is being mobilised (Anker et al. 2016; Keuschnig et al. 2021). In 2020, the deep-seated, slow-moving landslide measuring > 170,000 m² comprised > 1,700,000 m³ according to rough estimations (Keuschnig et al. 2021; Hermle et al. 2022). While an increasing movement rate was observed over the period 2018-2020 (Hermle et al. 2022), the number and size of exposed bedrock areas also rose in the following years. The material transported to the cirque threshold by sliding processes has been increasingly transferred further into the Obersulzbach Valley via debris flows since 2005. In 2014 the largest debris flow event, mobilising approximately 170,000 m³, caused severe damage in the Obersulzbach Valley (Anker et al. 2016; Keuschnig et al. 2021).

A precise investigation of sediment dynamics is essential for assessing potential hazards and future developments as well as incorporating this knowledge into mitigation strategies (Zhang et al. 2021). Locally, the quantification of mobilizable sediment volume and the input into the Obersulzbach allows proper dimensioning of the planned additional consolidation lock at the valley mouth to protect the Salzach Valley (Anker et al. 2016). The relevance for the Hohe Tauern National Park is evident in terms of the touristic utilization of the Obersulzbach Valley. The road along the debris cone at the foot of the Sattelkar is a highly frequented route for accessing the glacier trail and the mountain hut “Kürsinger Hütte”. In addition to the passability of the path, the potential disturbance of the nearby mountain pastures highlights the broader impact of debris flows on the national park's outer zone. In a broader perspective, data availability on sediment storage in cirques, sediment exhaustion of landslides and their activity development is limited, thus requiring further research. Therefore, this work aims to answer the following research questions:

(i) How does the sediment availability vary in different sliding scenarios within the study area?

(ii) What temporal trends are observed in the sediment dynamics of the sliding area and debris cone?

(iii) When does sediment exhaustion occur in the active slide of the Sattelkar cirque?

Addressing these aspects involves a quantification of current and potential mobilisable sediment volumes based on geometric interpolation of bedrock. Change detection using a time series of a digital terrain model (DTM) from 2012 and seven digital surface models (DSMs) between 2018 and 2023 allows the spatial and quantitative investigation of sediment dynamics in the cirque and the debris cone. By extrapolating the linear trend of the sediment discharge of the sliding area a timeframe of sediment exhaustion is estimated. In this study, the term “sediment exhaustion” marks the transition from a strong discharge to a neglectable sediment availability and therefore does not include further discharge of small amounts of sediment.

The following section serves as an introduction to the topic by reviewing the current state of research on high mountain landscapes and sediment storage analysis. Chapter three provides an insight into the study area. This is followed by a description of the data and procedures used to answer the research question. The fifth chapter deals with the results of the study, which are discussed and critically assessed in the following section. Finally, the findings are summarised and recommendations for further research are given.

2 Scientific framework

This chapter explains the theoretical foundations and the current state of research on processes and landscape forms in alpine regions. A particular focus is placed on the storage and depletion of sediment in general and in the context of landslides.

2.1 Geomorphological characteristics and processes in high mountain landscapes

High mountain landscapes are complex areas due to their heterogeneity and diverse geomorphological processes and landscape forms. Mountain ranges serve as the most important sources of sediment and water. Closely linked process systems transport these resources from the mountains to the lowlands and thus also strongly influence the landscape outside their source areas (Otto 2006).

These landscapes are characterised by geomorphological features such as altitude, steep slopes, rock outcrops, recent or quaternary glaciation, snow deposits (Troll 1966; Barsch & Caine 1984), the consequential climatic and vegetative zonation and diversity as well as tectonic activity (Barsch & Caine 1984). The geomorphological features also favour high precipitation and low temperatures, which promote metastable conditions regarding sediment balance and enhanced process activity (Owens & Slaymaker 2004). The process activity can be analysed using the power law concept (e.g. Hovius et al. 1997; Hartmeyer et al. 2020; Zhang et al. 2021), which states that processes of high intensity have a higher return period than small events.

Past processes are reflected in the resulting landforms and serve as a foundation for subsequent processes. As they are reworked, they act as a source of sediment and may have an inhibiting effect (Otto 2006). A characteristic landform in high mountain areas are cirques. Most of these are glacial paraboloidal hollow forms (Pedraza et al. 2019), which are delimited at the top by steep slopes >35° and are open at the bottom at the cirque threshold (Evans and Cox 1974). According to Evans and Cox (1974), the slope gradient within the cirque floor is usually <20°. Effective subglacial erosion on the flat to overdeepened cirque floor and superficial frost action on the upper cirque back wall lead to the typical profile of glacial cirques (Benn and Evans 2010). However, usually, the morphology is complex (Benn and Evans 2010; Pedraza et al. 2019; Jin et al. 2020). Numerous factors influence the formation and shape of cirques. Among these, the pre-glacial relief, glacial prehistory, lithology, rock structure and climate must be emphasised (Haynes 1968; Evans 2009; Benn and Evans 2010; Paasche 2011; Sanders et al. 2013; Pedraza et al. 2019).

The number of studies on the erosive behaviour of cirque glaciers and the resulting subsurface formations is limited. Many analyses are based on the simplified assumption of a rotating body derived from glacier flow measurements by Lewis (1960). Yet studies at West Washmawapta Glacier, Canada, refute this assumption (Sanders et al. 2018). The basal shape over a longitudinal profile can be described for 81 % of the circles using the k-type curve (Haynes 1968):

$$y = k(1-x)e^{-x} \tag{1}$$

Hereby y describes the vertical extent, x the horizontal distance along the profile and k (k = [0.5;2]) the concavity. High k values represent overdeepened cirques with steep back walls, while at k = 0.5 the valley floor is flat (Figure 1; Haynes 1968). It can be assumed that subglacial sediments, which inhibit glacial deepening, strongly characterise the longitudinal profile. Due to sediment accumulation, vertical changes decrease with long-lasting glaciation, hence a temporal variable must be considered (Evans 2009).

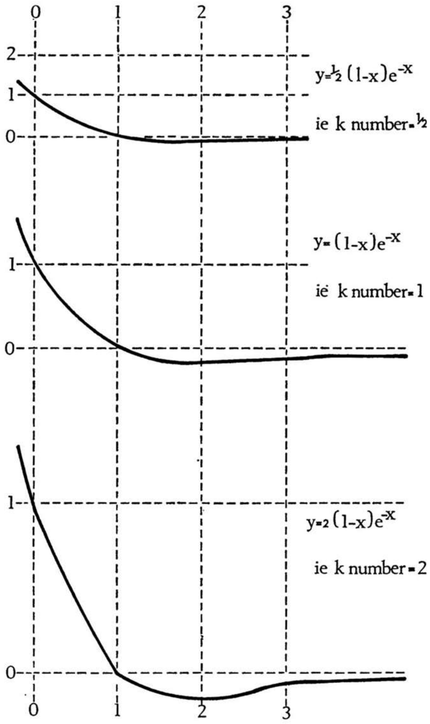

Figure 1: Ideal k-curve of a cirque (Haynes 1968).

Concerning the horizontal extent, a dependence on the geology and pre-glacial landforms is evident. Crystalline rocks and parallel fractures promote a broad formation of cirques with a length-to-width ratio < 1, whereas lithologies of metamorphic origin and fluvial catchment areas cause elongated cirques (Pedraza et al. 2019). An allometric development also leads to a temporal dependence of the morphometry. With increasing glacial imprinting, denudation in length and width intensifies (Evans 2009).

A more precise investigation of the subsurface structures is possible using geophysical measurement techniques, which detect the glacier bed or the bedrock either punctually or along profiles.

However, as the purpose of the investigations is often to quantify the glacier volume, medium to large glaciers are favoured over cirque glaciers in surveys (Grab et al. 2021). Accordingly, there is little data available on the rock morphology of cirques. An airborne ground penetrating radar (GPR) survey of Urbini et al. (2017) provides information on the bedrock of the Sforzellina cirque glacier in the Ortler Alps, Italy (Figure 2). In the transversal profile ridges and channels with height differences of up to 15 m are visible. The morphology exhibits soft transitions. The longitudinal profile shows an overdeepening of the cirque, in which the cirque has partly lower elevations than the cirque threshold. Since the longitudinal profile covers just the lower half of the glacier at a small ice tongue no information about the depth in the vicinity of the headwall is available (Figure 2; Urbini et al. 2017). The ice thickness profile of larger glaciers differs markedly from that of the cirque glacier in terms of a predominance of large, intensively pronounced subsurface structures over small channels and ridges. Grab et al. (2021) compare the glacier bed by GPR analyses with modelling on medium to large Swiss glaciers. As shown in Figure 3, the GPR measurements differ only slightly from the modelling. However, the modelling shows a stronger smoothing of subsurface structures and strong variations between the two models (Figure 3).

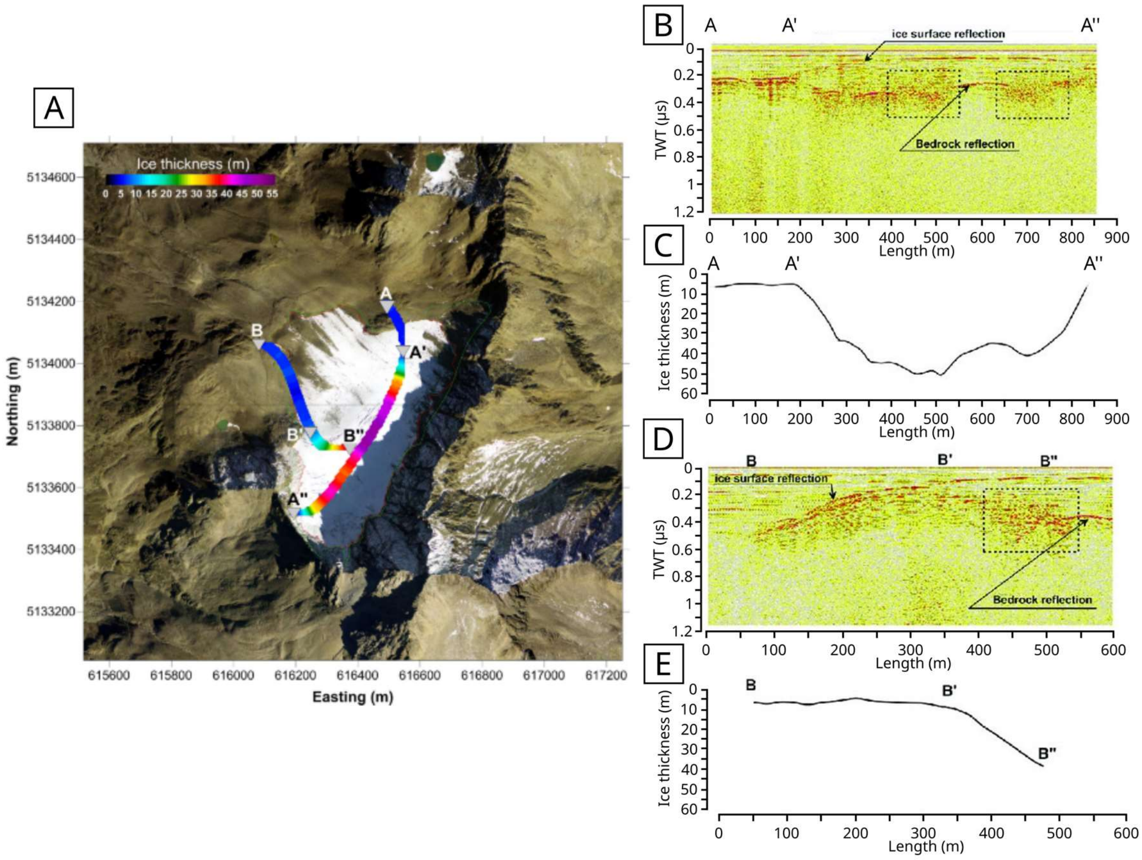

Figure 2: (a) Map of ground penetrating radar (GPR) profiles carried out at Sforzellina glacier. (b) Radargram of the transversal profile and (c) its conversion into ice thickness. (d) Radargram of the longitudinal profile and (c) its conversion into ice thickness (Urbini et al. 2017).

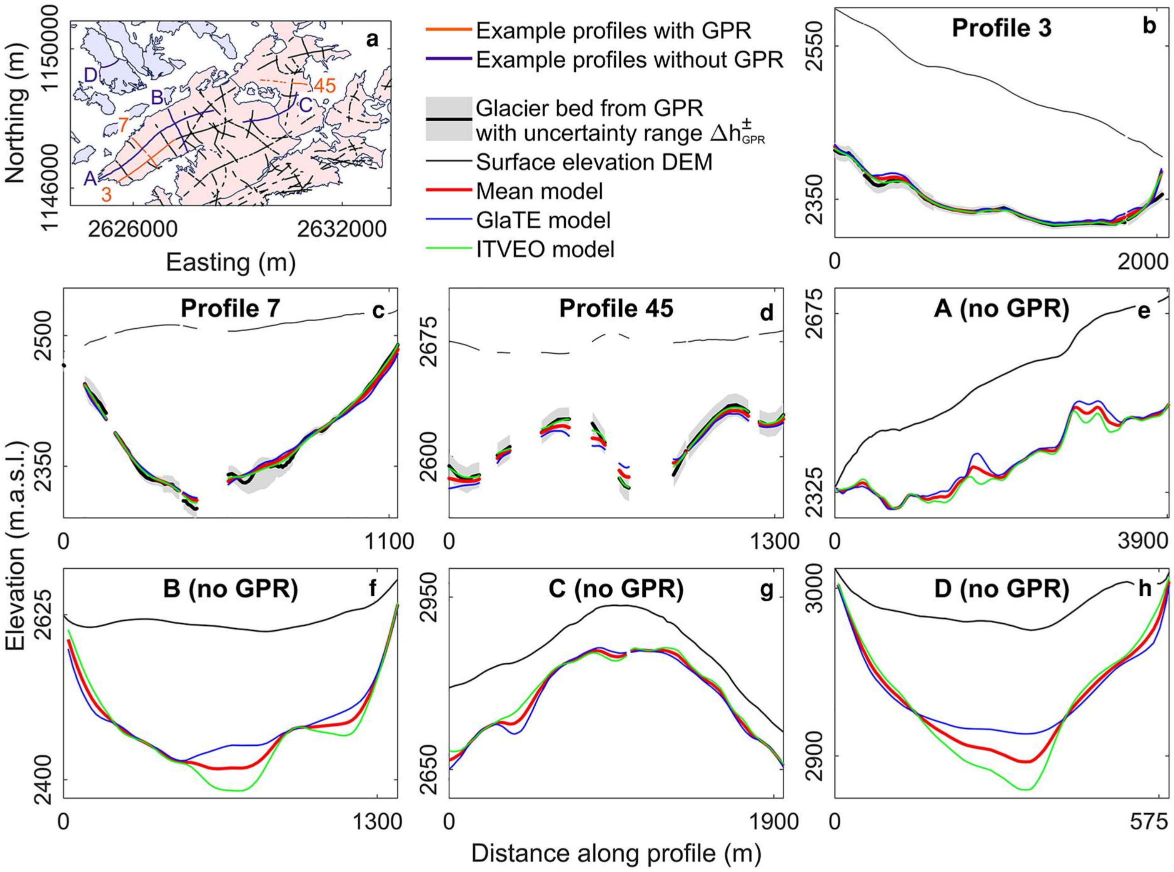

Figure 3: Comparison of glacier bed elevations through GPR measurements with the models GlaTE and ITVEO as well as their mean. (a) Overview map illustrating the shown GPR profiles (orange), different GPR profiles (black) and other transects (purple). (b)–(d) Comparison of glacier bed elevations of models and selected GPR profiles. (e)–(h) Comparison of modelled glacier bed elevations of profiles without GPR data (Grab et al. 2021).

Glacial hollows represent accumulation areas of loose material in the form of fine-grained to coarse-grained sediment. The cirque floor, moraines, debris cones, scree slopes as well as rock glaciers serve as intermediate storages of rockfall deposits and till, which are paraglacially reworked as the subsurface conditions change. Deposition takes place via the alluvial system in alluvial fans, debris cones or alluvial valley fills located below the cirque threshold (Ballantyne 2002). The methodology and temporary course of this paraglacial sediment cascade are presented in detail in Chapter 2.2.1.

2.2 Sediment storage analysis

2.2.1 Paraglacial models

The term “paraglacial” is used by Church and Ryder (1972) to describe processes that are not glacial but are nevertheless caused by the past presence of glaciers. Proglacial processes are also included here. Ballantyne (2002) extended the description of surface processes to sediment accumulations, landforms, land systems and landscapes.

The first mention was made by A. Godard in 1965, who used “paraglacial” to describe post-glacial landforms and their dynamics (Mercier 2008). Church and Ryder (1972) and Church and Slaymaker (1989) characterised the topic through their description of landscapes and processes in glacial and post-glacial landscapes in Canada. The investigations show a long-lasting increased process activity in the late glacial, which asymptotically approaches glacially undisturbed sediment loads with the complete retreat of the glacier (Figure 4; Church and Ryder 1972). The reason for this is a loss of stability during deglaciation, whereby unstable to metastable terrain is susceptible to the effects of superficial denudation processes (Church and Ryder 1972; Ballantyne 2002).

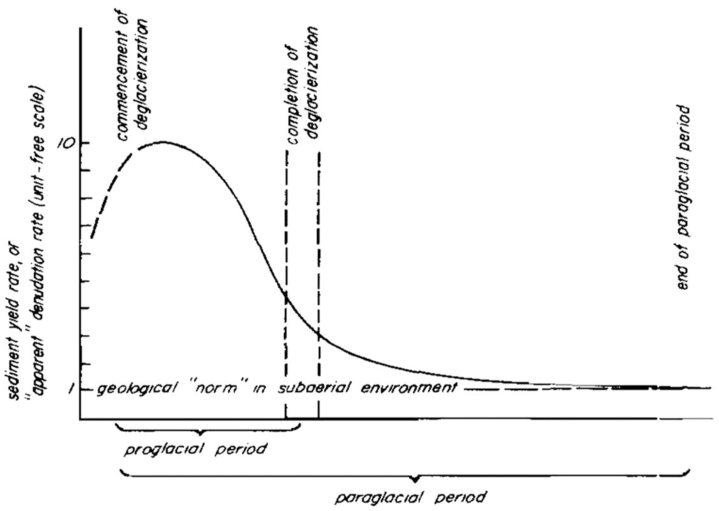

Figure 4: Schematic visualisation of the sediment yield of the paraglacial period (Church and Ryder 1972).

Based on their conceptual approaches, a paraglacial sediment cascade was established by Ballantyne (2002) that reflects postglacial landscape development and sediment transport. Thereby, six paraglacial landscape systems are formed, ranging from formerly glaciated valleys to marine depressions. These include rocky slopes, sediment-covered slopes, the glacier foreland as well as lacustrine, alluvial and littoral systems (Ballantyne 2002).

Important in cirques are rocky slopes, sediment-covered slopes and the alluvial system in the transition from the cirque threshold to the valley floor. Small-scale rockfalls, rock deformations and slope failures affect rock slopes over time periods of 100 - > 10,000 a and lead to debris accumulation. In permafrost areas, they also serve as the basis for the formation of rock glaciers. Sediment-covered slopes with gradients > 30° are susceptible to slope failure, debris flows, snow avalanches, tributary streams and surface washouts, which operate over a timeframe of 10 - 100 a. The erosion rates in paraglacial channels range from 0.001 m/a to 0.01 m/a (Ballantyne 2002). These processes lead to a reduction in slope inclination and concavity (Ballantyne and Benn 1994). The alluvial system ensures the fluvial discharge of sediment from the cirque bottom into downstream sediment sinks (Ballantyne 2002). Paraglacial alluvial systems are represented by debris cones, alluvial fans and alluvial valley fills. According to Ballantyne and Benn (1994), reworking processes of glacigenous sediments occur > 10,000 a in these systems.

The model of Ballantyne (2002) represents the basis for further concepts that attempt to integrate the complexity of the paraglacial sediment cascade. Cossart and Fort (2008) criticise this model at the beginning of the paraglacial phase. Due to the sediment retention of paraglacial landforms, especially moraine ridges, a delay in the maximum sediment accumulation occurs (Cossart and Fort 2008). The conceptual approach of Cossart and Fort (2008) therefore incorporates links between glacial and gravitational landforms and temporal aspects. According to Knight and Harrison (2018), the unidirectional assumption with universal landforms and depositional horizons of Ballantyne (2002) does not reflect reality. Instead, the paraglacial landforms interact with each other in complex relationships. Their development and degradation influence sediment yield and meltwater availability throughout the entire paraglacial phase (Figure 5). As the landscapes do not generally strive for a Davisian equilibrium, no constant low sediment yield is achieved over time (Knight and Harrison 2018).

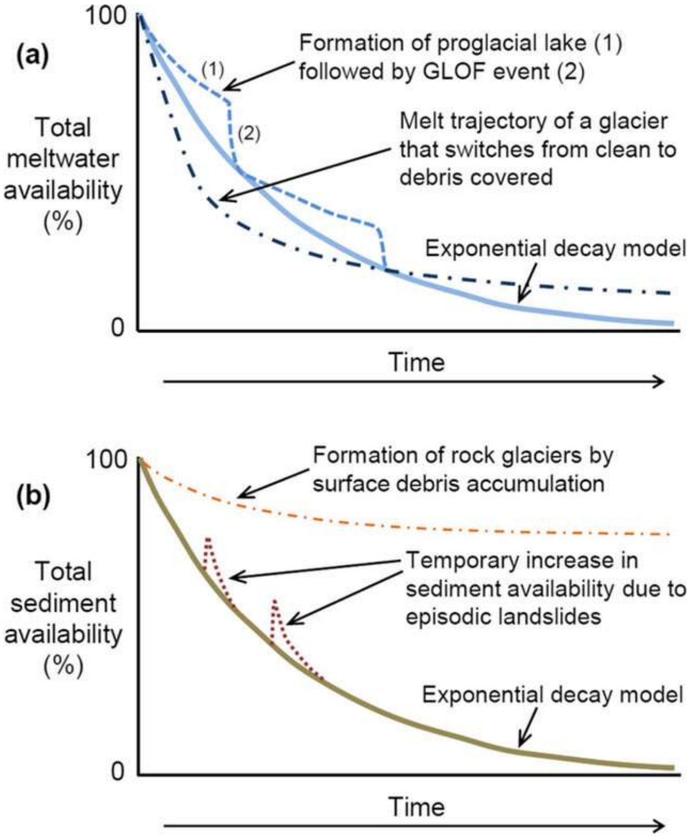

Figure 5: Paraglacial exhaustion model for the availability of (a) meltwater and (b) sediment in a paraglacial mountain system. 100 % corresponds to the total initial amount and 0 % to the total depletion (Knight and Harrison 2018).

A central aspect is the discussion of the duration of paraglacial processes. Ballantyne (2002) defines the paraglacial period as the period in which glacially influenced sediment availability is present. Once this point in time is reached, paraglacial sediment depletion occurs.

Ballantyne (2003) describes the exponential decrease in sediment availability during the entire paraglacial period through:

$$S_t = S_a e^{-\lambda t} \tag{2}$$

where S_t is the available sediment at time t, S_a is the available sediment at $t = 0$ and λ represents the rate of sediment loss (Ballantyne 2003 after Otto 2006). The time of sediment exhaustion can therefore be calculated by solving the equation 2 for t and setting $S_t = 0$.

Due to interruptions in the sediment cascade, disagreement exists about the temporal extent. The spatial location and size of the study area play a significant role here. Initially, Church and Ryder (1972) assumed that depletion occurs after a few thousand years. Church and Slaymaker (1989) limited this period to proximal areas, whereas in larger basins sediment availability begins later, continues to this day and therefore extends beyond 10,000 years. However, reworking can demonstrably take place in distal regions after > 100 ka (Blöthe and Korup 2013; Hoffmann 2015). The different periods emphasize the necessary differentiation between individual processes and the spatial correlation. Glacial sediments and those exposed by deglaciation are recurrently reworked. Therefore, it is questionable whether the paraglacial period ever ends on a large scale before the sediments are incorporated into a new paraglacial cycle during a glacial advance (Hoffmann 2015).

Paraglacial models are closely linked to analyses of sediment storage, connectivity and exhaustion of high-mountain environments. These studies comprise various spatial expansions reaching from landforms over catchments areas to mountain ranges (e.g. Hinderer 2001; Schrott and Adams 2002; Otto et al. 2009; Hoffmann et al. 2013; Hoffmann 2015; Schoch-Baumann 2022). Hereby, long time periods covering several thousand years are considered.

2.2.2 Sediment availability of landslides

The term sediment exhaustion is usually associated with paraglacial models, in which long periods are examined. The model by Knight and Harrison (2018) addresses the deviation of exponential sediment depletion due to disturbing factors. These also include mass movements. As illustrated in Figure 6, a transient increase in sediment availability followed by an exponential decline due to reworking and removal occurs.

Limited literature directly addresses sediment storage analyses of small basins and the dynamics of sediment exhaustion caused by landslides. The study by Chen et al. (2020) on temporal activity of seismically triggered landslides depicts an alternative perception of sediment exhaustion. These mass movements, occurring in the highlands of Sichuan, China, encompass moderate to very fast-moving landslides composed of rock, soil, and debris, primarily with shallow sliding surfaces. Their findings reveal a logarithmic decline in landslide activity, with sliding activities decreasing at lower rates than toppling processes (Figure 6). Regeneration processes with an increase in vegetation initiate approximately 10 years post-event, whereas projections indicate that the areas can be classified as stable after 25 years (Chen et al. 2020). Although the landslides do not entirely deplete all available sediment, the studied processes still reflect a degree of exhaustion. Due to stabilisation, the quantity of available sediment diminishes to pre-sliding levels. Consequently, a parallel can be drawn to the paraglacial model of Knight and Harrison (2018).

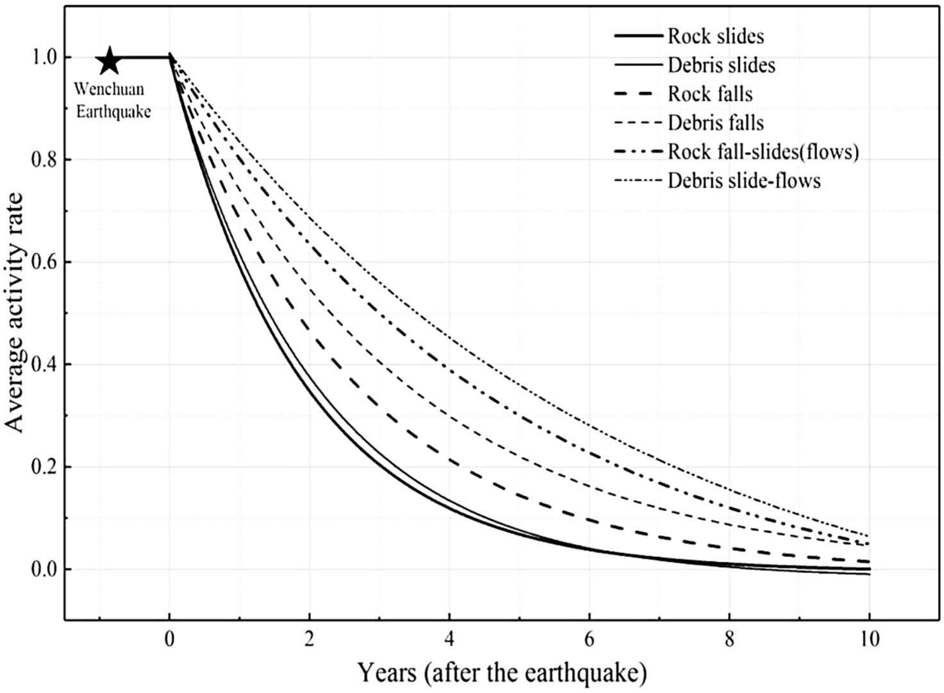

Figure 6: Activity decay of six types of landslides (Chen et al. 2020).

3 Study Area

This chapter firstly provides a geographical overview of the Obersulzbach Valley, focussing on the Sattelkar cirque. Subsequently, climatic, hydrological and geological conditions are presented. The geomorphological conditions depict a central component of the chapter.

3.1 Geographical overview

The Sattelkar is a west-exposed glacial cirque in the central area of the N-S-oriented Obersulzbach Valley. The sedimentary backfill of the cirque floor (~ 400,000 m²) extends from 2120 to 2750 m.a.s.l., whereas the cirque back wall reaches up to 2903 m.a.s.l. (Figure 7). The Sattelkar can be assigned to the municipality of Neukirchen am Großvenediger in the province of Salzburg and lies within the special protection zone of the Hohe Tauern National Park (NPHT) (Figure 7). The valley floor below is part of the outer zone of the NPHT (Hohe Tauern National Park 2018). Due to the protection zone and poor accessibility, the Sattelkar alone has a minimal anthropogenic imprint. The valley floor, on the other hand, is used for grazing. Due to the location of the Großvenediger and Großer Geiger peaks as well as numerous cirque and valley glaciers at the head of the valley, the Obersulzbach Valley is a popular excursion destination.

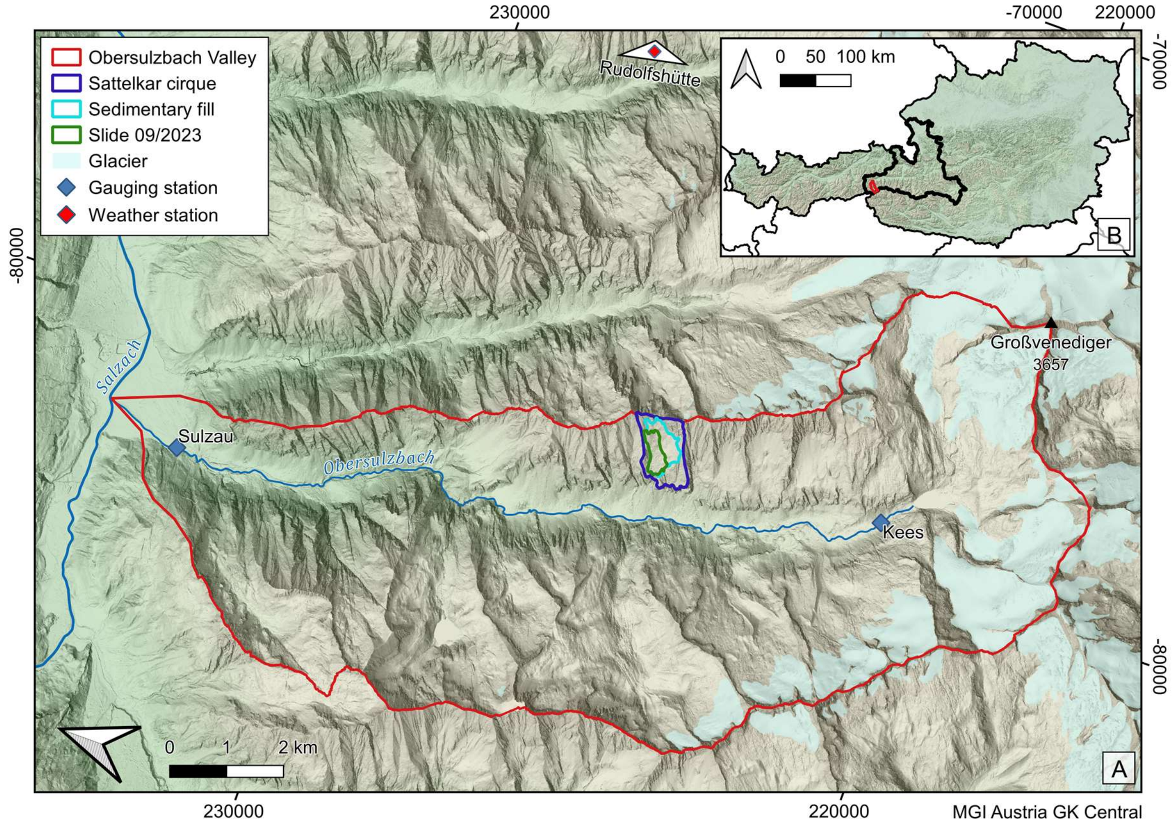

Figure 7: (a) Geographical overview of the Obersulzbach Valley and Sattelkar with (b) large-scale localisation of the study area (Data: geoland.at; Lieb et al. 2012; EfrainMaps 2020; BEV 2021; Land Salzburg 2023a; Land Salzburg 2023b).

3.2 Climate and hydrology

Temperature and precipitation impact geomorphological processes intensely. Thus, an analysis of the climate and hydrology of the Obersulzbach Valley is relevant. Due to insufficient data from the weather station at the Kürsingerhütte in the Obersulzbach Valley, the data from the semi-automatic weather station “Rudolfshütte” (GeoSphere Austria 2024a) is used for the long-term description of the climate data. This location may be considered comparable due to its location 26 km ESE of the study area and an altitude of 2320 m.a.s.l. (GeoSphere Austria 2023), which corresponds to the lower half of the Sattelkar sediment fill. Measurements of the water levels and discharge of the Obersulzbach river are taken at the “Kees” gauging station (2040 m.a.s.l.) below the Sulzsee in the upper reaches and at the valley mouth in the Sulzau (882.2 m.a.s.l.). The catchment area of the survey mark “Kees” amounts to 19.2 km² (BML 2023). Due to its location in the vicinity of several glaciers, their runoff contributes to the measured discharge in large parts. The Sattelkar is located approximately in between both gauging stations. The gauging station “Sulzau”, with a catchment area of 80.7 km², captures the runoff of the study side. Its values are therefore referred to in order to describe the hydrological characteristics of the Sattelkar (BML 2023).

According to Köppen (1936), the climate can be categorized as ET - an ice climate of the tundra - as the average mean temperature of the warmest month is between 0 °C and 10 °C. The average annual mean temperature is 0.1 °C (GeoSphere Austria 2023). In addition, the climate is characterized by year-round humidity (Figure 8). The annual total of precipitation fluctuated between 1548 mm and 2978 mm in the period 1993-2022, with a mean of 2393 mm. The maximum precipitation in 24 hours averages 72 mm (GeoSphere Austria 2023).

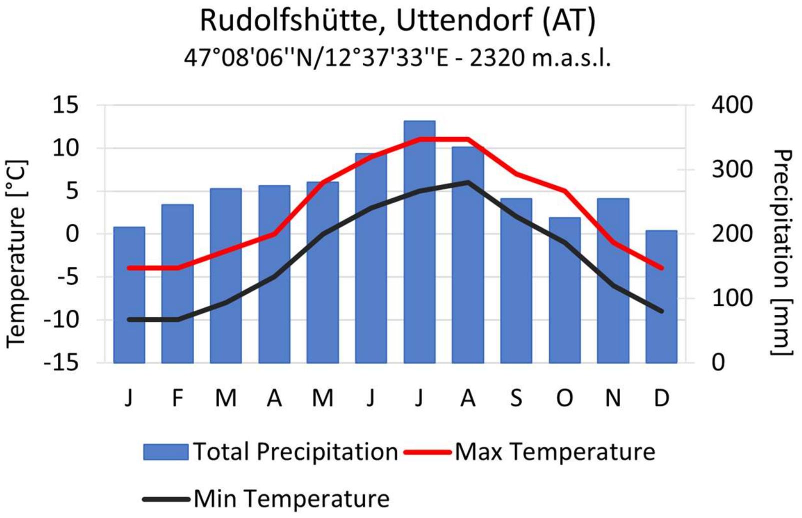

Figure 8: Climate diagram Rudolfshütte (Data: GeoSphere Austria 2023; MeteoNews AG 2024)

Additionally, the climatic trend is of importance to contextualize future evolution. The development of the average annual temperature in the period 1993-2022 shows a strong increase in temperature, which is also subject to strong fluctuations. The average 24-hour precipitation sum shows a slight positive trend, whereas the annual total precipitation is falling scarcely (Figure 9; GeoSphere Austria 2023).

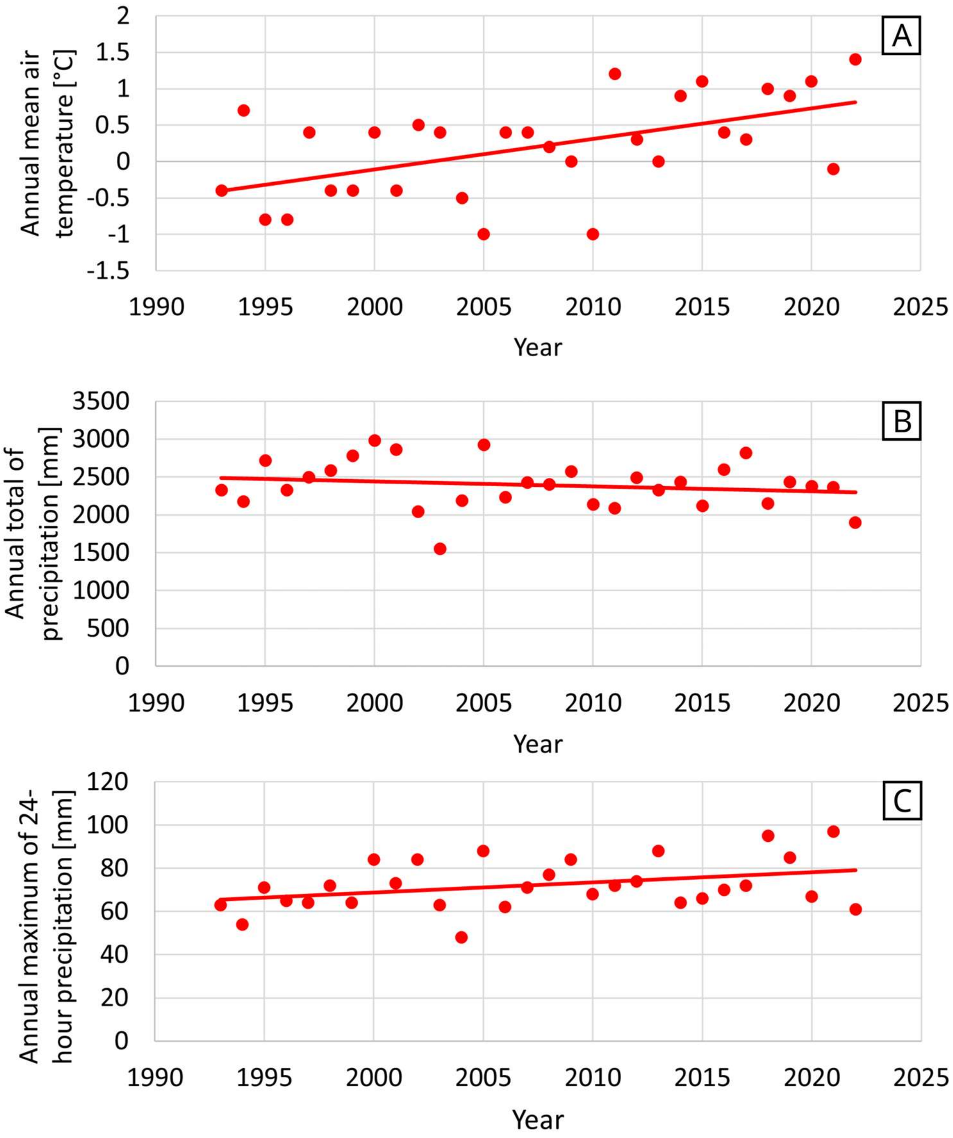

Figure 9: Annual (a) mean air temperature, (b) precipitation sum and (c) maximum 24-hour precipitation in the period 1993-2022 and its linear trend from the weather station “Rudolfshütte” (Data: GeoSphere Austria 2023).

Considering the hydrology, the Sattelkar catchment (> 800.000 m²) drains into the Obersulzbach via three streams. This torrent is mainly fed by the glaciers at the head of the valley and other tributary waters. The Obersulzbach runs along the valley floor of the same named valley and flows into the Salzach downstream of Sulzau. Historical records show that persistent flooding problems have been happening in Sulzau for a long time caused by the Obersulzbach (Anker et al. 2016; Land Salzburg 2023). Floods in this area are favoured by heavy precipitation lasting more than 12 hours up to high altitudes together with already prevailing wetness. Warming and the resulting snowmelt likewise influence this (Anker et al. 2016).

Data of the discharge measurements at the Sulzau measuring point cover the period 1961-2019. During this time, the highest discharge values were measured on 31 July 2014 with 129.0 m³/s. At the Kees measuring point, the maximum discharge on this day amounted to 21.1 m³/s and represents the fourth-highest monthly maximum in the period 1981-2019 (BML 2023). As the maximum 24-hour precipitation sum already occurred on 30 June 2014 (GeoSphere Austria 2023), it can be assumed that the high discharge on 31 July 2014 is the result of persistent precipitation and the outburst of the Obersulzbach after being dammed by a debris flow originating from the Sattelkar (Anker et al. 2016).

3.3 Geology

The Sattelkar consists of glacial till and bedrock assigned to the Penninic, whereas the valley floor is made up of quarternary loose debris. Augen- and flaser gneiss form the back wall, sill and flanks of the Sattelkar. The sedimentary fill consists of glacial till (Figure 10; Karl and Schmidegg 1979). The back wall of the cirque represents the origin of the rock fragments it contains, which means that the sediment also consists of central gneisses. Field investigations prove a wide range of grain size distribution from silt to blocks with diameters of 10 m. Outside the landslide area, the sediment is partly covered by a few decimetres of thick, shallowly rooted soil. In some places, depositions from rockfalls many decades ago can be found in the form of unrounded blocks with lichen growth.

The valley floor below the Sattelkar is composed of quaternary slope debris deposits (Figure 10). Due to changes in geomorphological process activity, several new debris cones have formed since the sector of the geological map was recorded in 1943-1946 (Karl and Schmidegg 1979).

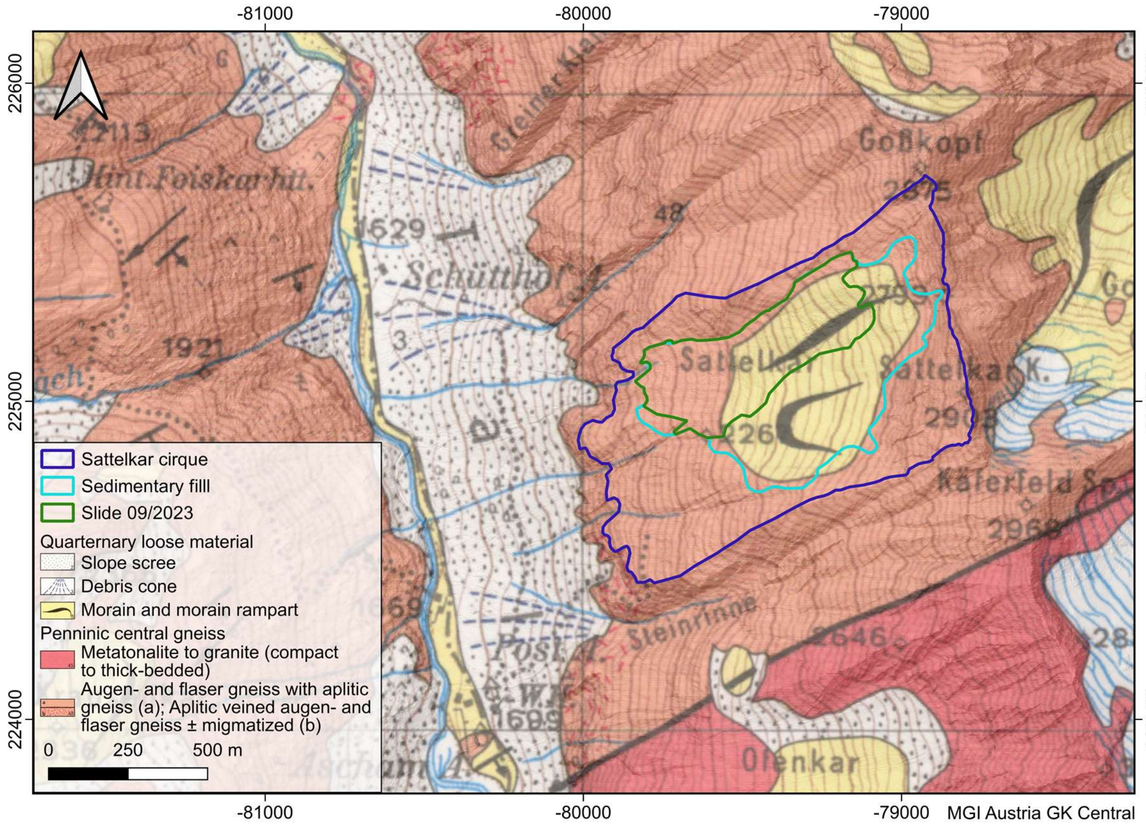

Figure 10: Geological map of the study site (Basemaps: geoland.at; Karl and Schmidegg 1979).

3.4 Geomorphology

The Obersulzbach Valley is distinguished by its glacial history. The glacial character is emphasized by a trough shape of the valley with high-lying cirque shoulders, numerous recent non-glaciated cirques as well as cirque and valley glaciers at the valley head. Distinct moraines in the southern part of the valley are the result of several glacial advances and stagnation phases (Anker et al. 2016).

The Sattelkar, a glacial cirque, experienced its last glaciation during the late Ice Age (Otto et al. 2018). The cirque floor, which is filled with sediment, has a mean slope of 32.6° as of September 2023. This steepness results from minor erosion during a brief glacial period, lacking significant deepening. Thus, a rather vaguely pronounced threshold is visible. Its glacial history is marked by a distinct headwall towards the east and several moraine walls (Karl and Schmidegg 1979; Otto et al. 2018). In addition to till, scree and rockfall deposits can be found within the hollow form (Otto et al. 2018). Subsurface exposures also show an increased proportion of fine material between the blocky deposits. The sediments are integrated into a fossil rock glacier to the NE of the cirque (Lieb et al. 2012), which can be seen in the 2003 orthophoto in the form of a tongue-shaped edge with vegetation cover in the upper half of the slide (Figure 11). Therefore, several glacial landforms and corresponding materials are apparent in the Sattelkar.

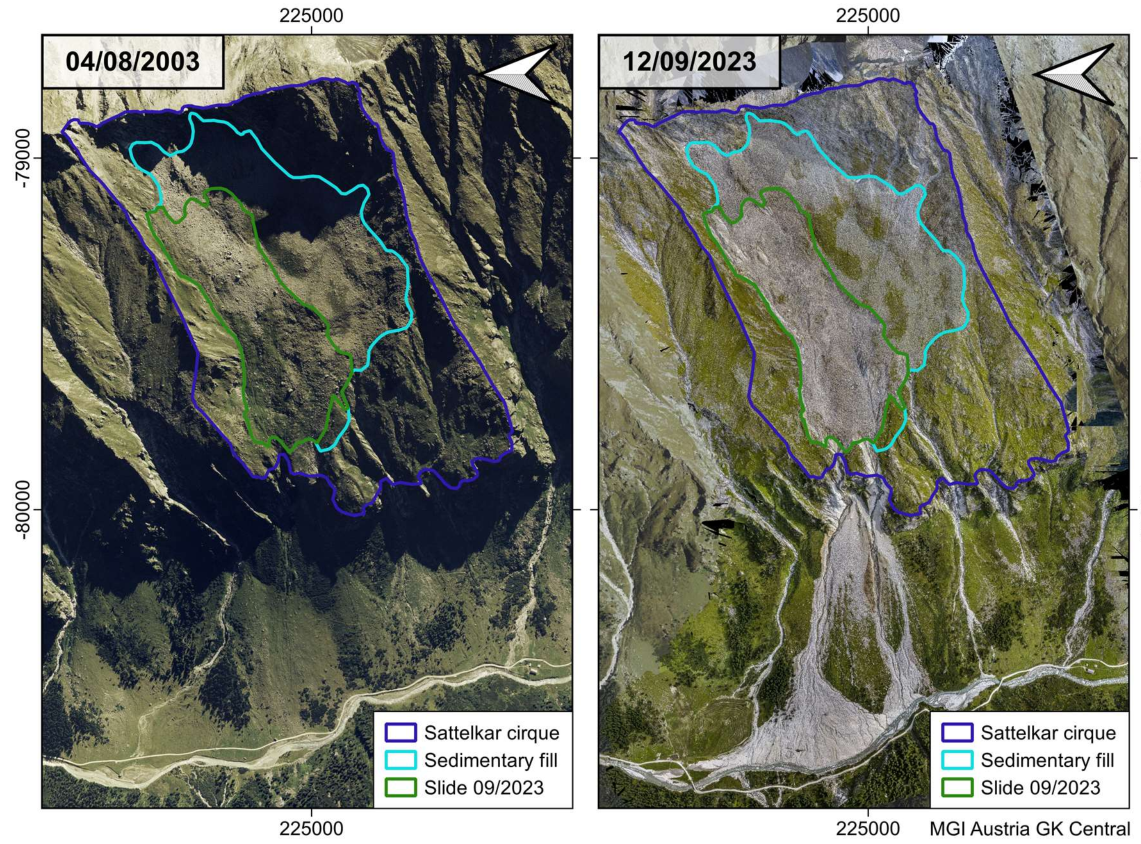

Figure 11: Orthophotos of the year 2003 (left) and 2023 (right) highlighting the changes in the Sattelkar cirque and debris cone underneath (Data: GEORESEARCH; Land Salzburg 2023).

Since 2005 a sliding activity in the northern part of the Sattelkar is detectable. Due to a progressively backwards moving headscarp reaching up to 2,600 m.a.s.l. in 2023, the debris of the rock glacier is integrated into the landslide and is not distinguishable anymore (Figure 11). In addition to a retrogressive displacement of the headscarp, lateral regression is visible directly at the landslide boundary as well as several meters SW of the active area in the form of cracks in the topsoil (Figure 12). The landslide displacement reached up to 30 m/a in the years 2012-2015 and a movement of 34.8 m/a was detected in the frontal part in 2019. Nevertheless, it needs to be mentioned that the displacement velocity differs a lot depending on the location within the landslide area. The highest displacements take place in the frontal part and channels in the northern part of the moving area (Hermle et al. 2021). Based on the classification according to Zangerl et al. (2008), the Sattelkar landslide can therefore be categorized as a slow-moving landslide. In the period from 2010 until 2023 a maximum elevation change of about 20 m occurred. The remobilization towards the frontal part led to an exposure of several well-smoothed bedrock ridges in the south-western, northern and south-eastern parts of the landslide body. These outcrops underline the glacial history of the cirque. Simultaneously, the occurrence of bedrock within the landslide emphasizes the locally shallow distribution of bedrock. As no investigations were carried out regarding the course of the sliding surface, neither a reliable statement can be made about the depth progression, nor the existence of a rotational or translational sliding movement.

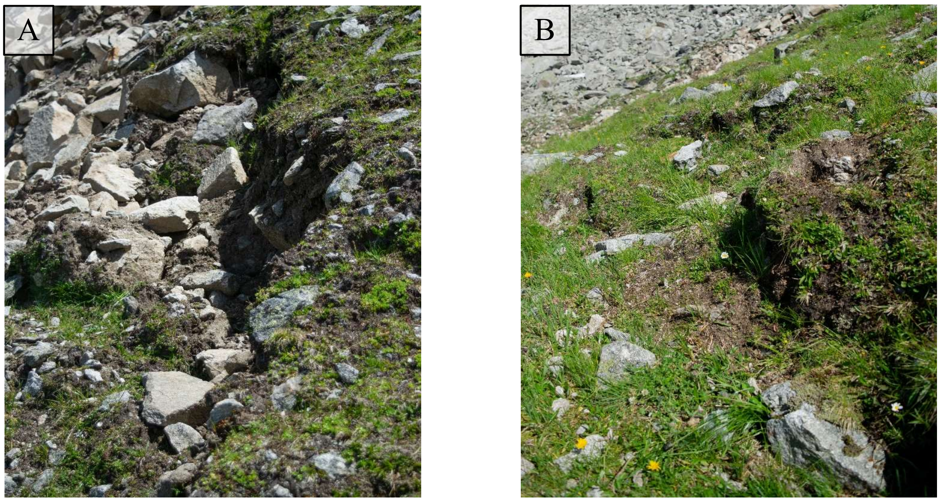

Figure 12: Lateral headscarp retreat in form of (a) an integration of material at the southern boundary of the landslide and (b) surface cracks approximately 5 m SW of the lateral boundary indicating slow movement. Both pictures were taken 07/2023.

Permafrost degradation is considered a possible instability factor in the Sattelkar. According to the topoclimatic key, permafrost occurrence in steep slopes (>11°) and rock is only possible from 2700 m.a.s.l. (Schrott et al. 2012). As a result, the Permakart 3.1 permafrost model does not show any permafrost deposits in the sediment fill except for small areas (Data: Otto et al. 2020). However, five out of six temperature loggers installed by GEORESEARCH Forschungsgesellschaft mbH (GEORESEARCH) at a distance of 100 m laterally to the active landslide indicate sporadic permafrost due to negative temperatures at the base of the winter snowpack. Within the three-year study period from 1 January 2016 to 31 December 2019, a slight warming trend from -1.1 °C to -0.6 °C was observed (Keuschnig et al. 2021).

Loose debris moved towards the threshold depicts the source of material for reoccurring debris flows connected to heavy precipitation. The biggest event took place on 30th/31st July 2014 and led to the initial movement of a 0.4 km² measuring debris cone with similar dimensions to those of the current one. In total about 170,000 m³ of material were transported, where of 70,000 m³ originated from above the threshold of the Sattelkar cirque and 100,000 m³ were reworked scree (Anker et al. 2016). In combination with other mass relocations in the rear Obersulzbach Valley and heavy precipitation the debris flow of the Sattelkar caused a temporary damming and subsequent relocation of the drainage channel (Anker et al. 2016), a flooding of the whole Obersulzbach Valley and destruction of the middle and lower reach of the Obersulzbach (Keuschnig et al. 2021). Additionally, smaller events since 2010 led to a further reworking of sediment (Chapter 5.3).

4 Methods

This study's methodological approach encompasses sediment storage and surface change analysis, alongside sediment exhaustion time prognosis. Potentially mobilizable sediment was assessed via sub-surface bedrock interpolation and elevation difference modelling between surface and bedrock. Multi-temporal digital elevation models (DEMs) serve as a basis for the calculation of height differences by DEM of Differences (DoDs). Erroneous vertical displacements within DEMs, evident in DoDs, were quantified and are considered in volume calculations of accumulation, denudation and balances Moreover, trends in annual net change were computed to extrapolate sediment depletion time for five landslide scenarios.

4.1 Sediment storage analysis

Sediment storage analysis depicts a key element for further processes in quantifying sediment exhaustion. The most accurate subsurface information to determine sediment volumes originates from shallow geophysical surveys, such as electric resistivity tomography, ground penetrating radar or refraction seismic (Hoffmann and Schrott 2002; Otto et al. 2008). Nevertheless, the accessibility of alpine terrain as well as a low penetration depth in sediments with high electrical conductivity and many near-surface reflectors (Ahnert and Schrott 2015) impede the application of geophysical methods. Further approaches are geometric and statistical analysis, core drilling and the usage of high-resolution surface data (Schoch-Baumann 2022).

The quantification of sediment volumes was carried out through a combined application composed of (i) mapping of surface bedrock out of high-resolution orthophotos, (ii) linear low-order polynomial regression of these bedrock outcrops, (iii) three-dimensional subsurface interpolation and (iv) a volume determination between the subsurface-bedrock and the sediment surface.

4.1.1 Geometric subsurface interpolation

Subsurface interpolation is divided into two sub-steps: (i) The two-dimensional interpolation by low-order polynomials and (ii) the three-dimensional generation of a subsurface terrain model by "Topo To Raster", integrated into the geographic information system software ArcGIS Pro (Figure 13).

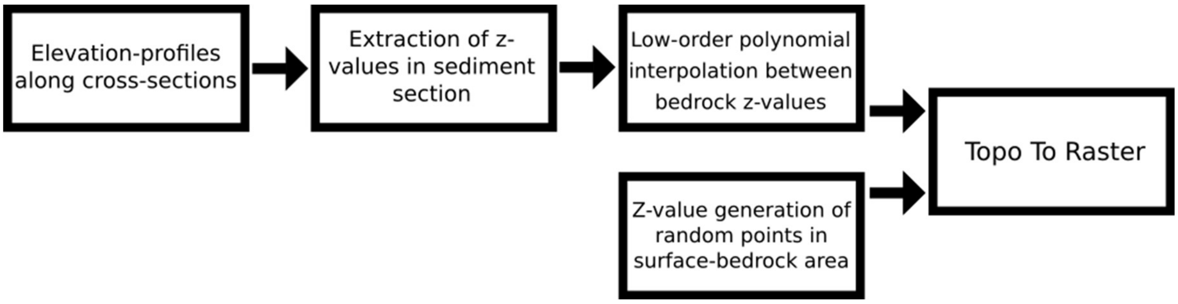

Figure 13: Workflow of bedrock interpolation.

The polynomial interpolation was executed in Excel along four transversal and six longitudinal cross-sections evenly distributed in the cirque to gain more data points in the central parts of the cirque (Figure 14). Elevation profiles along the cross-sections provide the z-values of the near-surface bedrock. Polynomials can be used to interpolate the depth profiles of the bedrock in between. When selecting the polynomials, preference was given to those that have the lowest polynomials and yet run below the sediment surface. It was also taken into account that the elevation values in the intersection area of the interpolated polynomials match each other. In the event of greater deviations, the values of the geomorphologically more plausible interpolations were preferred.

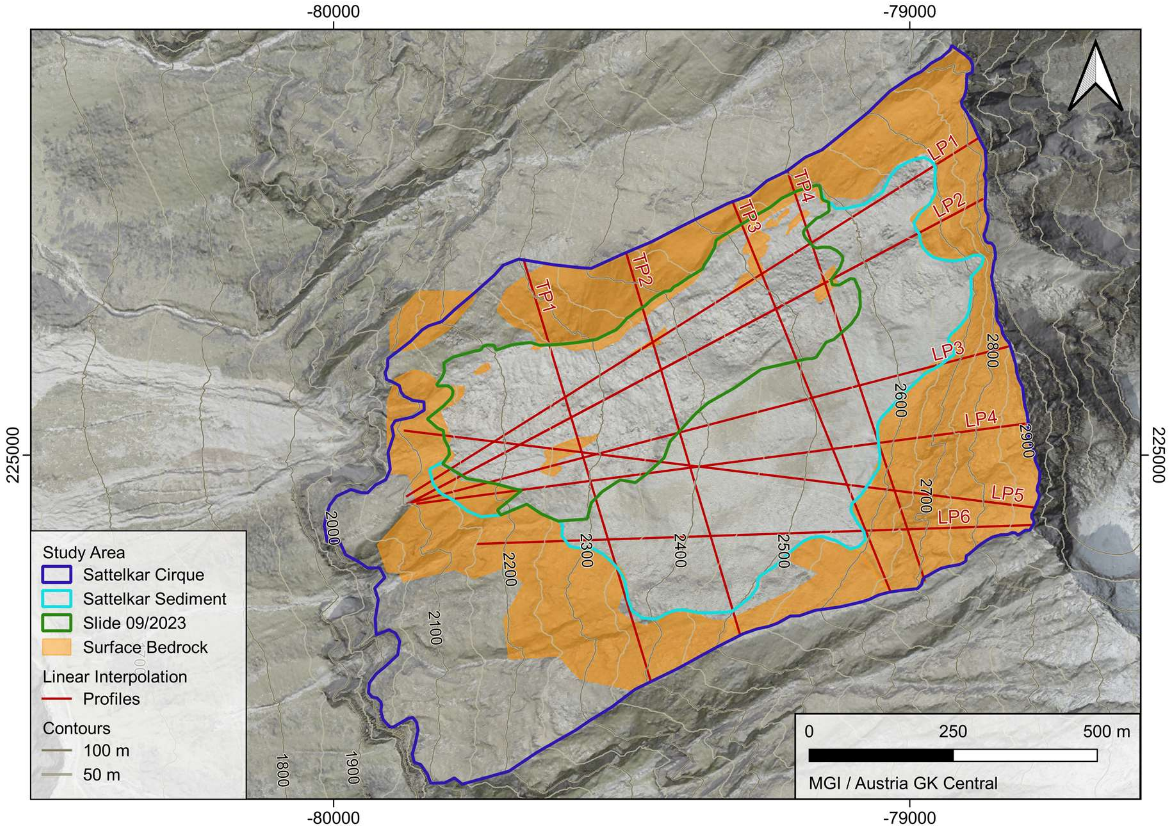

Figure 14: Geographical localisation and labelling of the cross-sections and superficial bedrock deposits used for the bedrock interpolation (Basemaps: geoland.at)

In addition to the linear interpolations, the basis for the areal interpolation of the rock is formed by the altitude values of exposed rock surfaces in the landslide area, the surrounding cirque walls and the cirque threshold as well as in areas in which near-surface rock distribution can be assumed. The data density accounts for a minimum of 5 m to ensure smooth data processing. Due to a local inaccuracy at the boundaries of the sediment filling additional bedrock locations needed to be embedded to guarantee a course underneath the sediment surface in large parts. The used interpolation method “Topo To Raster” depicts a tool integrated into ArcGIS. This algorithm is based on ANUDEM by Michael Hutchinson (Hutchinson 1988). Version 5.3 of ANUDEM is currently used in ArcGIS Pro (Esri 2021). This tool aims to represent hydrologically correct topographic surfaces including ridges and drainage channels (Esri 2021). It allows several different types of input data such as points, contours or streamlines (Esri 2021; Hutchinson 1988). An iterative finite interpolation technique using Gauss-Seidel iterations is implemented in “Topo To Raster” (Hutchinson 1988).

A comparison of “Topo To Raster” to other interpolation methods by Unger (2012) underlines, that this method is the most suitable for the generation of terrain models of the glacier sub-surface. Since the Sattelkar cirque has a comparably high inclination gradient it can be assumed that the base of the cirque is not deeper than the threshold. Nevertheless, glacial erosion can lead to an incompletely developed drainage network. Thus, the better-fitting sub-surface bedrock model was chosen in which no drainage was enforced.

4.1.2 Volume quantification

The volume quantification is based on the subtraction of the interpolated bedrock from the surface elevation data, each with a spatial resolution of 1 m. Negative values of the resulting sediment thickness were assumed to depict surface bedrock by setting the thickness to 0 m. The zonal statistics tool of QGIS allows the calculation of volumes by multiplying the interpolated sediment thickness of each pixel by the area of the layer. Apart from the whole sediment filling of the Sattelkar cirque, the volume was calculated for five different scenarios (Sc1-Sc5) (Figure 15).

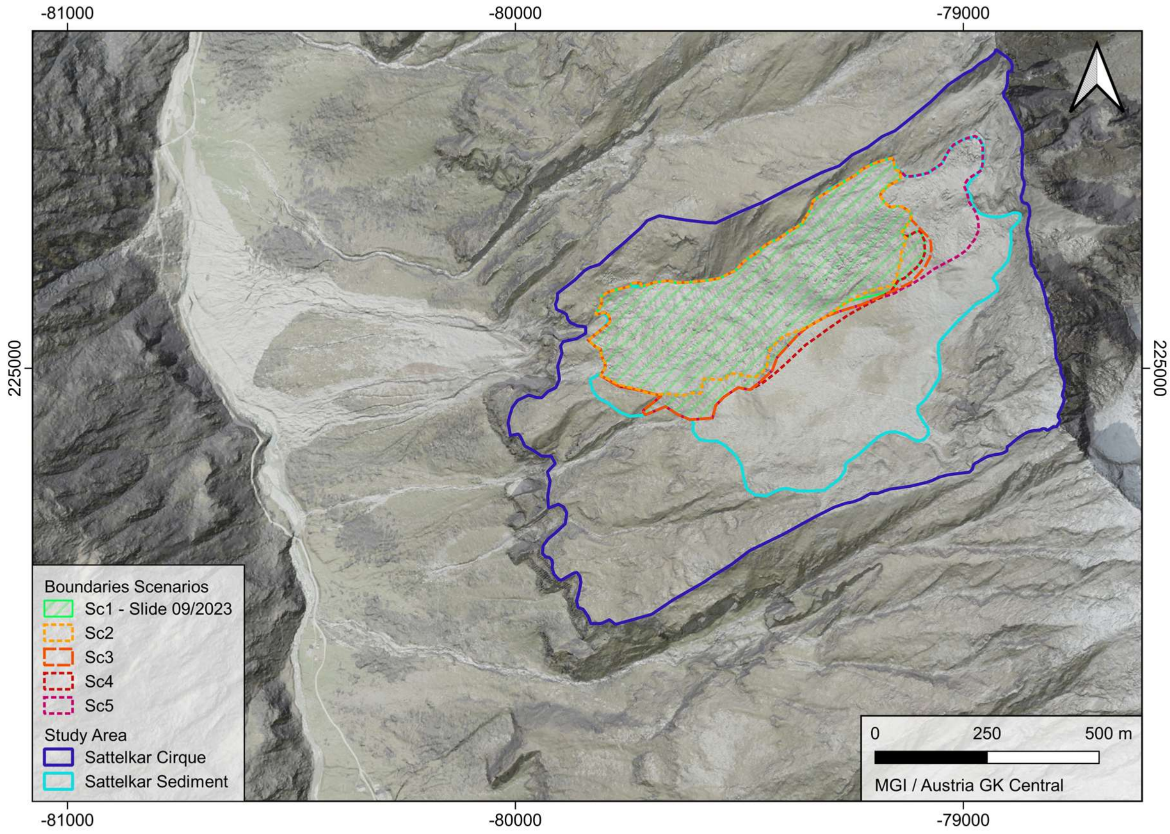

Figure 15: Geographic overview of the different sliding scenarios Sc1-Sc5 (Basemaps: geoland.at).

These scenarios represent different sliding areas with the simplified assumption of a sliding surface between the sedimentary filling and bedrock. Sc1 represents the sliding area in September 2023, whereas Sc2-Sc5 depict the potential evolution of the sliding area. The area in Sc2 is based on Sc1, yet those southwestern areas that have shown little change in movement in recent years were omitted. Sc3 and Sc5 are areas with a low (Sc3) or high (Sc5) headscarp retreat. The mobilization of a frontal moraine at the southern boundary of the sliding is the basis of Sc4.

Elevation data sets from three different times were used: 07/2022, 07/2023, and 09/2023. The data of 09/2023 is used to gain knowledge about the volume, which is stored in the different scenarios these days. The mean values of the volumes of 07/2022 and 07/2023 serve the determination of the sediment depletion time and are depicted as simplified values for 01/2023.

Due to the interpolation and an assumption of the sliding surface of the landslide at the bedrock-regolith transition, an uncertainty range exists, which is set to 5 %. In addition to quantifying the sediment volumes of all scenarios and periods, the respective values were also determined with a deviation of ± 5 %.

4.2 Analysis of surface changes

4.2.1 Data

A digital terrain model (DTM) and multiple digital surface models (DSMs) serve as the foundation for surface change analysis (Table 1). The DTM of August 2012 was generated by an airborne laser scannig (ALS) flight on behalf of Land Salzburg (2012). The digital surface model (DSM) data acquisition was carried out by GEORESEARCH using the unmanned aircraft system (UAS) DJI Phantom 4. Each survey consists of four flights, which were launched at different altitudes. The flight planning was carried out with the software UgCS while maintaining a high overlap (front 80 %, side 70 %) and a target ground separation distance of 0.04-0.08 m.

Table 1: Digital elevation models (DEMs) used to calculate the interpolated sediment thickness and surface changes. All data was provided by GEORESEARCH. The digital surface models (DSMs) originate from UAS flights by GEORESEARCH, the digital terrain model (DTM) from an ALS flight on behalf of Land Salzburg (2012).

Type	**Date**	**Spatial resolution**
DTM	22.08.2012	1.00 m
DSM	13.07.2018	0.08 m
DSM	24.07.2019	0.08 m
DSM	09.07.2020	0.08 m
DSM	21.07.2021	0.06 m
DSM	19.07.2022	0.06 m
DSM	18.07.2023	0.06 m
DSM	12.09.2023	0.04 m

4.2.2 Error determination

The DEMs exhibit a vertical error δz, which is also reflected in the calculation of DoDs, due to deviations such as tilting or displacement of the point clouds relative to each other. These errors propagate themselves in the quantification of volume changes and their derivations. It is therefore necessary to minimize and quantify these errors. Due to the enormous processing power required and a possibly only small error reduction despite a considerable additional effort, which would go beyond the scope of the work, the point clouds were not referenced in this work. However, the systematic errors were determined to identify the Minimum Level of Detection (LOD_{Min}) and enable the inclusion of errors in the volume calculation and trends.

Since the vertical error of each DEM is not known, a determination of the combined error in the DoD using the root sum square of errors was not possible. Instead, the vertical error δz of the

DoDs was determined manually. For each DoD, the vertical deviation was determined separately for the cirque and the sediment cone at 15 fixed points such as bedrock, old large blocks or the road. The mean DEM deviance and its uncertainty can be derived from this. Converted to the area, this also results in the mean volume deviance of each DoD concerning the landslide or debris cone.

The determination of the systematic error enables a more detailed evaluation of the results in three ways. On the one hand, it is possible to determine LOD_{Min} and eliminate values in this error range. This value was set to 1 m based on the results of the error determination. Additionally, it is possible to deduce the volumetric extent to which the calculations of the sediment dynamics are over- or underestimated. To achieve a comparability of the values, a pixel-based error correction was carried out. For this, the volume deviance was determined separately for pixels indicating accumulation (δV_A) or denudation (δV_D). This allows the determination of corrected volumes, which are marked with the suffix "$_{corr}$" according to:

$$V_{b,corr} = V_a - (A_a * \delta z) \tag{3.1}$$

$$V_{b,corr} = V_d + (A_d * \delta z) \tag{3.2}$$

$$V_{b,corr} = V_a - 2 * \left((A_a + A_d) * \delta z\right) \tag{3.3}$$

where V_a, V_d and V_b are the accumulated, denudated and balanced volume and A_a and A_d are the areas of accumulation and denudation. Furthermore, the determination of the uncertainty of the mean volume deviance enables an error weighting of trends such as the error-weighted normalized balance. The error weighting w_i and generation of the trend was performed using R Studio based on an instrumental fit according to:

$$w_i = \frac{1}{\sigma_i^2} \tag{4}$$

where σ_i represents the uncertainty of the error bars (OriginLab 2024).

4.2.3 Data processing

The quantification of the sediment budget was carried out using DEMs of differences (DoDs). DoDs allow the quantification of volumetric changes between two topographic data sets within the same coordinate system by subtraction of the elevation data:

$$\delta E = Z_2 - Z_1 \tag{5}$$

where δE is the elevation change in each pixel between the DEMs at the times t_1 and t_2 according to its altitude information as Z_1 and Z_2 respectively. Hereby t_1 represents the recording time of the older DEM, whereas the newer survey took place at t_2 (Figure 16; Williams 2012). For this method, the raster calculator integrated in QGIS 3.28 was used. Equation 5 assumes that both DEMs represent the morphology realistically. Therefore, inaccurate values are initially also integrated into the DoD, which need to be eliminated for the quantification and visual illustration of alterations.

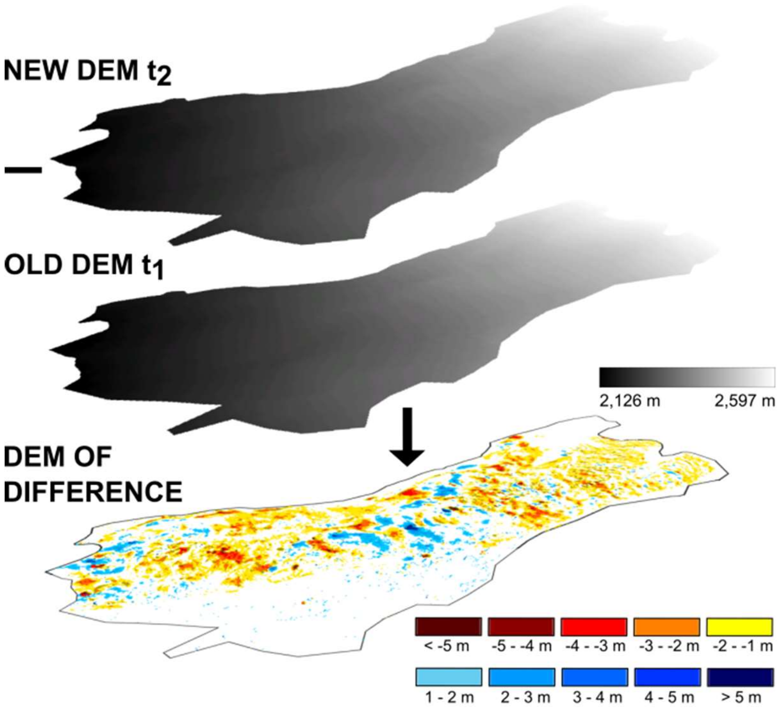

Figure 16: Schematic representation of the generation of a DEM of Difference (DoD). By subtracting the height value at time t_1 from the height value at t_2 on a cell-by-cell basis, a difference model is obtained.

The DoDs allow the quantification of volumetric changes over the LOD_{Min}. Summing up δE of each pixel quantifies the net change as balanced volume V_b. Additionally, separate values of the denudation V_d and accumulation V_a were estimated. Each quantification was normalized to annual values of volume change (V_{nb},V_{nd},V_{na}) and normalized rates (BR, DR, AR) based on the respective active area were determined. To achieve comparability the error-corrected values are always used throughout the thesis. The uncorrected values can be found in Appendix A-C.

The debris cone and the landslide area were analysed both individually and together. For the study periods between 2018 and 2023, the active area of September 2023 was used in each calculation. Due to a high variability in the stream network between 2012 and 2018, for 08/2012-07/2018 and 08/2012-09/2023 the active area of the whole periods is involved in the quantification. Even though the original spatial resolution of the DSMs reaches from 0.04 m to 0.08 m, a spatial resolution of 1 m was chosen for all data sets to maximize the comparability.

On a temporal basis, the main analysis examines annual differences from July to July. Additionally, the DoDs of 08/2012-07/2018, 07/2018-07/2023 and 08/2012-09/2023 aim to get an overview of spatial and quantitative mid-term sediment dynamics (Table 2).

Table 2: Investigation periods of surface change via DoD.

	Date	**Area**
July - July	13/07/2018 – 24/07/2019	cirque + debris cone
	24/07/2019 – 09/07/2020	cirque + debris cone
	09/07/2020 – 21/07/2021	cirque + debris cone
	21/07/2021 – 19/07/2022	cirque + debris cone
	19/07/2022 – 18/07/2023	cirque + debris cone
mid-term analyses	22/08/2012 – 13/07/2018	cirque + debris cone
	13/07/2018 – 18/07/2023	cirque + debris cone
	22/08/2012 – 12/09/2023	cirque + debris cone

4.3 Sediment exhaustion

Based on the previously calculated landslide volumes and superficial changes, the times of sedimentary depletion can be determined. Due to the short activity of the landslide, linear trends are better proxies than exponential development. Hence the linear trend of the net change V_{nb} in the sliding area, adapted to the period 08/2012 - 07/2023, is used to quantify sediment exhaustion. The remaining sediment volume V_r is calculated according to:

$$V_{r,t} = V_{r,t-1} + V_{nb,t-1} \tag{6}$$

The initial volume $V_{r,t=0}$ used for the predicted evolution is the mean sediment volume of 07/2022 and 07/2023, which represents the assumed volume for 01/2023. The time of sediment exhaustion is defined by the date on which $V_r = 0$. The sediment depletion time is calculated for all five development scenarios of the landslide surface. Furthermore, error propagations of the interpolation are included. For this purpose, the respective calculations include 5 % error ranges. These represent inaccuracies in future development due to an incorrect input value of the sediment volume.

Deviances by systematic errors due to inaccurate overlays of the point clouds of the elevation models are also considered. Therefore, in another calculation, the error-weighted trend of the normalized balance of the landslide was used to determine the sediment depletion.

5 Results

This chapter comprises the results of the executed sub-steps. Firstly, the outcomes of the bedrock interpolation and the derived potentially mobilizable sediment volumes are delineated. These are followed by the spatial and quantitative analysis of the sediment dynamics in the Sattelkar and the associated debris cone. At last, the time of sediment depletion is described.

5.1 Bedrock interpolation

The interpolation of the bedrock shape is essential for determining the available sediment volume and thus also the sediment depletion. The interpolation was carried out in two steps using linear interpolation and generating a three-dimensional elevation model of the rock course. As the linear interpolation only serves as an aid for the subsequent large-scale interpolation, only the final result is explained subsequently.

Across six longitudinal and transverse profiles, clear insights into interpolated subsurface structures and the bedrock's depth beneath the sediment surface are revealed (Figure 17). Within longitudinal profiles, varying subsurface structures are evident from north to south. In the northern profile, which intersects the active landslide area, the bedrock runs close to the surface or is even exposed. The maximum sediment thickness amounts to 18 m. Unlike the uniform slope of the sediment surface, the underground terrain exhibits several gentle terraces. Irregularities are also noted in LP-STK-Central. Towards the east, within a profile length of 70-200 m, the bedrock runs near the surface, displaying a flattening compared to the cirque's back wall (0-70 m). A distinct deepening occurs at 600 m along the profile. Intersections of linear interpolation profiles correspond to the positions of these edges. In the interpolation of the southern cirque, pronounced depressions are identified, reaching depths of up to 45 m below the sediment surface (Figure 17a). In Figure 17b a prominent ridge is evident in the TP-STK-West and TP-STK-Central profiles at a length of 300 m and 350 m respectively. In the west of the cirque, the bedrock is exposed at the surface. The area north of the ridge marks the active landslide area, which has a bowl-shaped form with smaller channels. This is likewise recognisable in the TP-STK-Central profile, yet less pronounced. A depression is also located in the south of the cirque, which is more prominent in TP-STK-Central. As in the longitudinal profiles, prominent ridges and depressions in this cross-section intersect the profiles of the linear interpolation. Concave and convex structures of various dimensions are also found in the upper third of the cirque. Major depressions are reached in the centre of the TP-STK-East profile (Figure 17b).

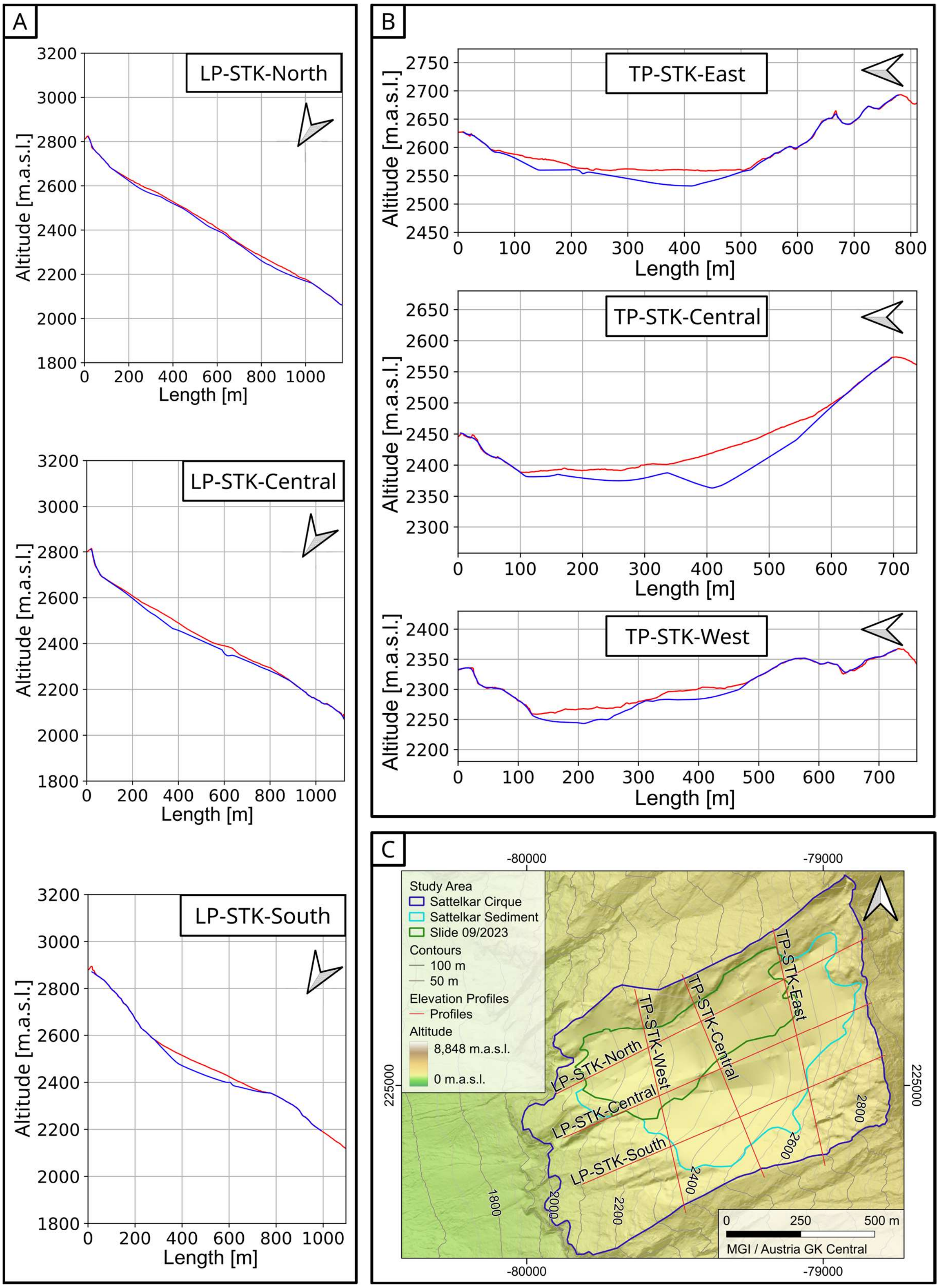

Figure 17: (a) Longitudinal and (b) transversal elevation profiles of the Sattelkar showing the interpolated bedrock distribution (blue) and the surface derived from the DTM (red). (c) DEM of the bedrock in the Sattelkar cirque and DTM of the surrounding surface. The red lines mark the studied elevation profiles of (a) and (b) (Basemaps: geoland.at; DTM: Land Salzburg 2012).

5.2 Sediment volume

Table 3 enhances our understanding of the entangled relationships between area, sediment volume, and mean sediment thickness across different sliding scenarios and depicts the values of the cirques' sediment filling. The uncertainty of the sediment volume represents a potential volume deviation of five per cent due to interpolation imprecisions. The analysis comprises the status quo of 09/2023 as well as the initial sliding volume used for the sediment exhaustion quantification. Latter are represented by the mean values of the results from 07/2022 and 07/2023 (Appendix D).

Table 3: Area (A), sediment volume (V) and mean sediment thickness of the sediment filling and the sliding scenarios Sc1-5 of the Sattelkar cirque. The determined values depict the status quo 09/2023 and the mean value of the times 07/2022 and 07/2023.

Time	Description	A [m^2]	V [m^3]	Mean Thickness [m]
09/2023	sediment filling of the cirque	383,520	6,003,880±300,194	14.8
	Sc1	184,385	1,245,838±62,292	6.8
	Sc2	165,549	995,722±49,786	6.0
	Sc3	188,703	1,314,371±65,719	7.0
	Sc4	191,683	1,400,318±70,016	7.3
	Sc5	223,016	1,786,140±89,307	8.0
Mean of 07/2022 and 07/2023	Sc1	184,385	1,274,414±63,721	6.9
	Sc2	165,549	1,023,789±51,189	6.2
	Sc3	188,703	1,341,739±67,087	7.1
	Sc4	191,683	1,428,810±71,441	7.5
	Sc5	223,016	1,800,240±90,012	8.1

The sediment volume of all scenarios varies between approximately 1,000,000 m^3 and 1,800,000 m^3. The lowest cubage exhibits Sc2, whose mean sediment thickness and area are also notably lower than those of the other scenarios. Sc4 shows only a slight increase in area compared to Sc3, yet the sediment volume is approximately 85,000 m^3 higher in Sc4. In the case of Sc5, both surface area and sediment volume increase significantly compared to Sc1-4. This leads to an intense alteration of the proportion of area and sediment volume. In all scenarios with strong relative volume changes (Sc2, Sc4, Sc5), noteworthy variations in the mean sediment thickness are apparent (Table 3).

The map of the sediment thickness of 09/2023 of the whole sedimentary fill of the Sattelkar cirque depicts a strong spatial variation. The thickest sediment cover is located in the SE of the cirque measuring approximately 62 m. The sediment thickness progressively declines towards the cirque margins. A reduction of sediment thickness can also be detected at the edges of the sliding area. The sediment is up to 28 m thick in the central part of the slide. The thickest sediment deposit within the overall sliding area is found towards the southern boundary, at the foot of the terminal moraine at an altitude of 2,360 m.a.s.l.. Here the maximum sediment thickness amounts to about 42 m. In the central part of the morain rampart outside of the active slide, the deposit reaches up to 50 m. With thicknesses in the ranges of up to 25 m the amount of stored sediment in the vicinity of the headscarp at the upper sliding boundary is also of importance (Figure 18).

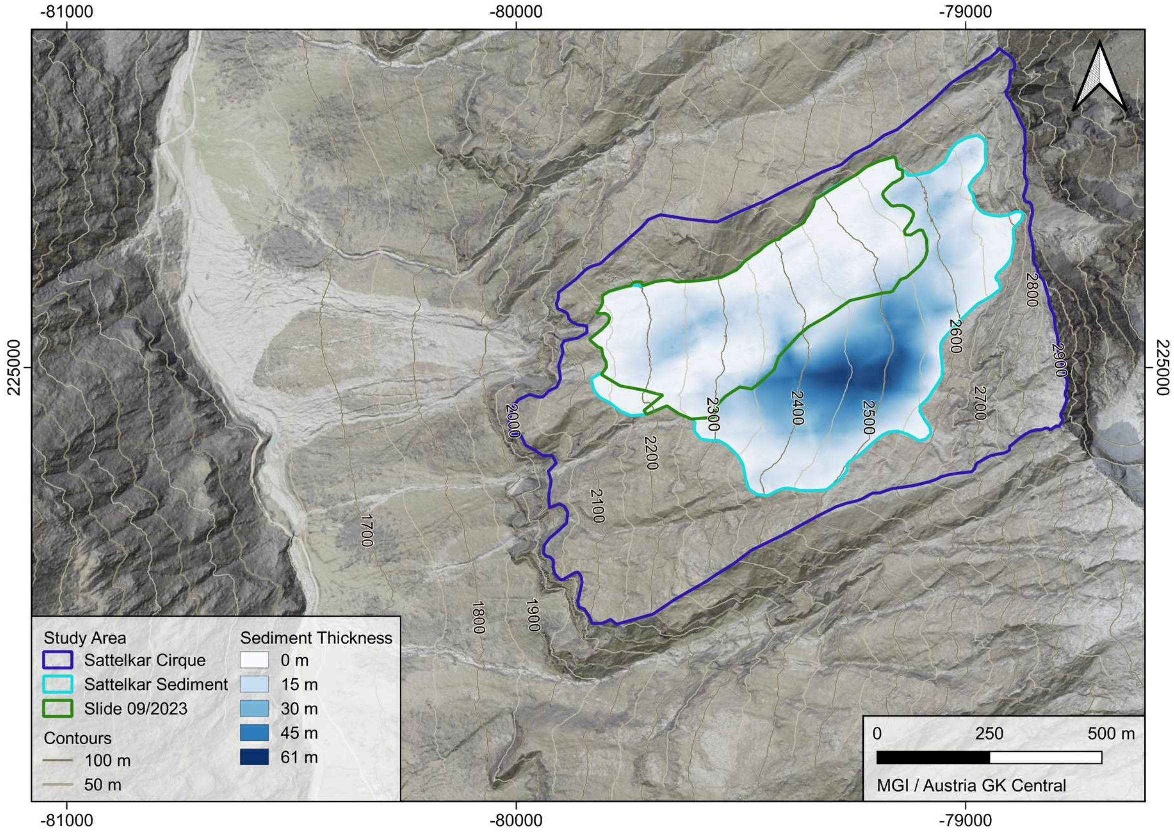

Figure 18: Thickness of the sedimentary fill of the Sattelkar in 09/2023 (Basemaps: geoland.at).

5.3 Surface changes

Surface changes within the slide and debris cone are essential to understand the dynamic evolution of this geomorphological feature. The overall goal of determining the surface changes in the investigated region is based on a multi-layered investigation. Firstly, the results of the quantified systematic errors in the derived DoDs are explained. The subsequent quantitative and spatial analysis of the surface changes in this chapter aims to decipher the dynamics that characterize the landscape in the period from 08/2012 to 09/2023. Studying the landslide area and the debris cone both together as well as individually enables the identification of patterns, trends and anomalies in surface changes. This approach helps to understand the complex interaction between the geomorphological processes and the key factors influencing the redistribution of sediments in this dynamic environment.

5.3.1 Error determination

Minor tilting and inaccurate overlapping of the point clouds of the DSMs lead to inaccuracies in the calculation of DoDs. The error determination aims to quantify the mean errors of the sliding area and debris cone.

As shown in Table 4, vertical deviations prevail across almost all analysed periods. There are significant differences between δz of the cirque and the debris cone. The strongest positive deviance in the landslide is at $\delta z = 0.56$ m in the DoD from 08/2012-07/2018 and the most negative in the subsequent period 07/2018-07/2019 with $\delta z = -0.47$ m. In four periods $|\delta z|$ is ≤ 0.15 m within the cirque, whereas this is only the case for the debris cone 07/2019-07/2020. The vertical deviations in the area of the debris cone range from $\delta z = -0.78$ m in 07/2019-07/2020 to $\delta z = 0.53$ m in 08/2012-07/2018. The uncertainties sometimes exceed 0.80 m in both sub-areas and frequently surpass the mean deviations.

Converting δz to the volume by multiplying the deviation and the uncertainties of the active area results in the volume deviation due to systematic errors. Additionally, the annual volumetric deviation is determined, which is of great relevance for the comparability of values. The normalized mean volume deviation shows an overestimation of up to around 18,000 m^3/a for the landslide area in the DoD from 07/2020-07/2021. The largest underestimation occurs in the period 07/2018-07/2019 with around 84,000 m^3/a. In the area of the debris cone, the annual volume deviations range from around -130,000 to 74,000 m^3/a (Table 4).

Table 4: Determined systematic errors of each DoD in the sliding area and debris cone as mean vertical deviance of the DoDs as well as total and annual mean volume deviance.

	Period	**Mean DEM deviance δz [m]**	**Mean volume deviance δV [m^3]**	**Normalized mean volume deviance δVn [m^3/a]**
Slide	08/2012-07/2018	0.56±0.51	97,870±88,893	16,607±15,084
	07/2018-07/2019	-0.47±0.78	-86,438±143,961	-83,910±139,749
	07/2019-07/2020	0.04±0.43	7,554±78,946	7,855±82,095
	07/2020-07/2021	0.10±0.81	18,576±150,462	17,984±145,673
	07/2021-07/2022	-0.12±0.13	-22,291±23,220	-22,414±23,347
	07/2022-07/2023	-0.24±0.17	-44,705±30,650	-44,828±30,734
	07/2018-07/2023	-0.44±0.41	-82,476±76,160	-16,441±15,182
	08/2012-09/2023	0.00±0.60	-606±110,433	-55±9,982
Debris cone	08/2012-07/2018	0.53±0.79	68,298±102,707	11,589±17,428
	07/2018-07/2019	0.36±0.84	57,603±134,354	55,918±130,423
	07/2019-07/2020	-0.78±0.83	-125,075±132,745	-130,064±138,040
	07/2020-07/2021	0.16±0.20	25,959±31,376	25,133±30,377
	07/2021-07/2022	0.11±0.26	18,450±41,031	18,552±41,256
	07/2022-07/2023	0.46±0.17	74,016±27,354	74,219±27,429
	07/2018-07/2023	0.35±0.54	56,531±86,888	11,269±17,321
	08/2012-09/2023	0.21 ± 0.43	35,180 ± 70,910	3,180±6,410

5.3.2 Spatial change detection

Examining the spatial distribution of annual sediment dynamics reveals distinct patterns within each time interval. In the periods 2018/2019, 2019/2020 and 2022/2023, low subsidence is apparent in the upper regions of the landslide, with few areas of >3 m height reduction. Only a small area is characterized by positive elevation change in 2018-2019. Large areas show just minor changes or slightly negative values. The lower half of the landslide area largely exhibits a height increase in 2019-2020 and only a small area with a negative height difference. In the 2022-2023 study period, height soars of up to 2 m also predominate in the lower landslide area. The debris cone shows linear patterns with differences of up to 5 m in the west during these periods. In the form of a gradual increase to the south, the DoD of 2019-2020 shows negative elevation changes that are not linked to prevailing channels. Apart from this, negative elevation changes can be observed in small parts of the debris cone. In contrast, the sediment dynamics in the study periods from 2020-2022 are more pronounced with positive and negative height differences >5 m at the debris cone and in the landslide area. In 2020-2021, a strong height decrease is evident in the upper two-thirds of the landslide. Except for a linear appearance of negative height differences at the northern edge of the landslide, positive values prevail in the NW of the cirque. In 2021-2022, the entire landslide area is predominantly characterized by a decrease in height, which is less pronounced in the upper area than in the lower half. Small-scale, yet distinct positive values can be found in the SW of the landslide. In both study periods the sediment dynamics at the upper debris cone are characterized by strong linear height reductions close to intense increase. Additionally, in the fan-like lower part, wide-spread areas of positive height differences can be found, which are strongly pronounced in 2020-2021 (Figure 19).

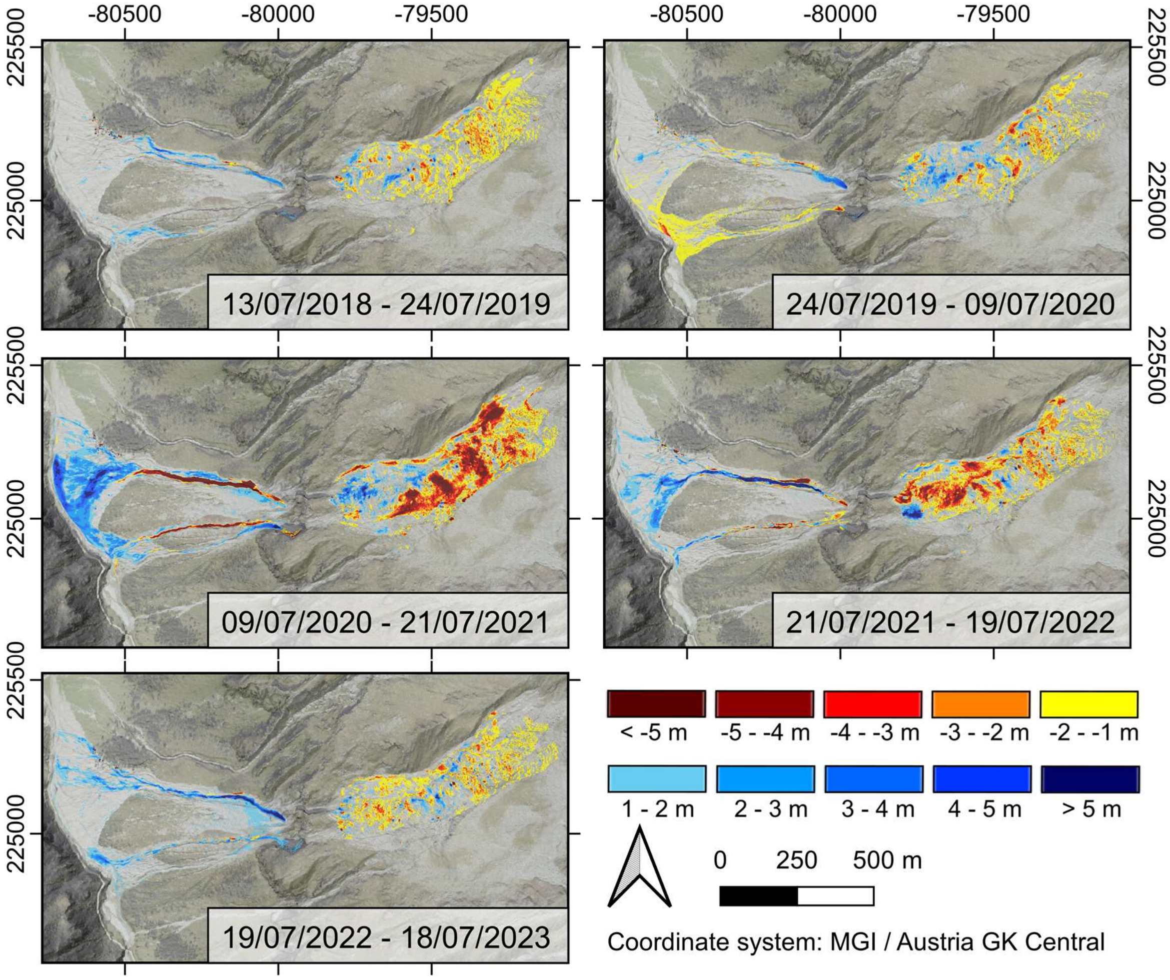

Figure 19: Non-error-corrected surface changes of the periods July to July of the years 2018-2023 (Basemaps: geoland.at).

5.3.3 Quantification of surface changes

Based on the findings of the spatial distribution of the height differences and the geomorphological process of sediment remobilisation, the quantifications are subsequently interpreted as follows: The summation of positive pixel values are labelled as accumulation volumes and negative pixels as denudation. Furthermore, these areas are considered combined as balance or net change.

5.3.3.1 Surface change of the sliding area and debris cone

A notable feature of the sediment dynamics in the combined area of the Sattelkar slide and the debris cone is the removal of approximately 170,000 m³ in 08/2012-07/2018. With over 570,000 m³ an even higher discharge is attributable to the last 5 years. The increased sediment dynamics since 07/2018 are also reflected in the separate analysis of annual accumulation, denudation and net change (Table 5).

Table 5: Volumetric surface change of the combined area of slide and debris cone including a pixel-based correction of the systematic error of DoDs covering mid-term analyses between 2012 and 2023.

Period	**Days of period**	**$V_{b,corr}$ [m³]**	**$V_{nd,corr}$ [m³/a]**	**$V_{na,corr}$ [m³/a]**	**$V_{nb,corr}$ [m³/a]**
22/08/2012 – 13/07/2018	2,151	-168,117	75,696	57,592	-28,528
13/07/2018 – 18/07/2023	1,831	-574,106	124,642	66,495	-114,445
22/08/2012 – 12/09/2023	4,038	-462,125	92,753	52,128	-41,772

$V_{b,corr}$ is the error-corrected volume of net change, $V_{nd,corr}$ of the annual denudation, $V_{na,corr}$ of the annual accumulation and $V_{nb,corr}$ of the annual net change.

Looking at the mean annual net change in the period 2022-2023, positive values prove a general accumulation of sediments in the study area. However, the spatial distribution of denudation and accumulation patterns reveal no indication of mass growth stemming from external inputs. Noteworthy negative balances were observed during the 2020-2021 and 2021-2022 periods. The peak of annual sediment transfer occurred in 2020-2021, marked by the highest values in both normalized denudation and accumulation. Likewise, 2021-2022 exhibited comparatively high denudation and accumulation (Table 6).

Table 6: Volumetric surface change of the combined area of slide and debris cone including a pixel-based correction of the systematic error of DoDs covering annual periods from July to July in 2018-2023.

Period	**Days of period**	**$V_{b,corr}$ [m³]**	**$V_{nd,corr}$ [m³/a]**	**$V_{na,corr}$ [m³/a]**	**$V_{nb,corr}$ [m³/a]**
13/07/2018 – 24/07/2019	376	-44,880	98,287	38,408	-43,567
24/07/2019 – 09/07/2020	351	-25,222	96,157	57,962	-26,228
09/07/2020 – 21/07/2021	377	-135,889	300,450	179,771	-131,564
21/07/2021 – 19/07/2022	363	-74,903	177,573	99,017	-75,315
19/07/2022 – 18/07/2023	364	6,121	81,165	88,239	6,137

$V_{b,corr}$ is the error-corrected volume of net change, $V_{nd,corr}$ of the annual denudation, $V_{na,corr}$ of the annual accumulation and $V_{nb,corr}$ of the annual net change.

5.3.3.2 Surface change of the sliding area

In the landslide area, approximately 920,000 m³ were removed from the cirque during the period 08/2012-09/2023. On an annual scale, this amounts to 83,000 m³/a. A higher negative annual net change in 07/2018-07/2023 compared to 08/2012-07/2018 is attributable to a recent strong increase in denudation. The accumulated volume has decreased by half but has only a minor impact due to its low value (Table 7).

Table 7: Volumetric surface change of the slide including a pixel-based correction of the systematic error of DoDs covering mid-term analyses between 2012 and 2023.

Period	**Days of period**	**$V_{b,corr}$ [m³]**	**$V_{nd,corr}$ [m³/a]**	**$V_{na,corr}$ [m³/a]**	**$V_{nb,corr}$ [m³/a]**
22/08/2012 – 13/07/2018	2,151	-421,503	66,094	6,075	-71,524
13/07/2018 – 18/07/2023	1,831	-478,790	111,350	3,188	-95,444
22/08/2012 – 12/09/2023	4,038	-919,300	85,013	1,917	-83,097

$V_{b,corr}$ is the error-corrected volume of net change, $V_{nd,corr}$ of the annual denudation, $V_{na,corr}$ of the annual accumulation and $V_{nb,corr}$ of the annual net change.

The time interval 07/2020-07/2021 is characterized by the highest normalized erosion and the most substantial negative normalized balance. In contrast, the lowest erosion and the highest accumulation are observed in 07/2019-07/2020, resulting in the second lowest balance on an annual basis (Table 8). Concerning the chronology of accumulation, denudation and normalized net change, a discernible pattern emerges in the annual analyses. When accumulation is low in a given year, the subsequent year exhibits low erosion, and vice versa, underscoring the interplay and cyclical nature of sediment dynamics within the sliding area (Table 8).

Table 8: Volumetric surface change of the slide including a pixel-based correction of the systematic error of DoDs covering annual periods from July to July in 2018-2023.

Period	**Days of period**	**$V_{b,corr}$ [m³]**	**$V_{nd,corr}$ [m³/a]**	**$V_{na,corr}$ [m³/a]**	**$V_{nb,corr}$ [m³/a]**
13/07/2018 – 24/07/2019	376	-26,332	79,008	18,646	-25,562
24/07/2019 – 09/07/2020	351	-32,218	68,643	37,478	-33,503
09/07/2020 – 21/07/2021	377	-221,608	239,527	35,045	-214,554
21/07/2021 – 19/07/2022	363	-113,758	149,309	25,211	-114,385
19/07/2022 – 18/07/2023	364	-35,434	71,963	22,054	-35,531

$V_{b,corr}$ is the error-corrected volume of net change, $V_{nd,corr}$ of the annual denudation, $V_{na,corr}$ of the annual accumulation and $V_{nb,corr}$ of the annual net change.

A pronounced variability over the periods is observable in the accumulation. The accumulated volume of all annual and long-term periods amounts to 16,000-36,000 m³, showing a low variation considering the time range of 1 to 11 years. Comparing the annual accumulated volume of all periods it becomes apparent that in mid-term analyses the values are remarkably lower (Table 7, Table 8).

When examining sediment dynamics, the normalized balance plays a particularly important role. In the data of the landslide area, it becomes clear that the numbers are always negative, indicating that sediment discharge outweighs sediment input (Table 7, Table 8, Figure 20). Only in the intervals from 07/2018-07/2020, the error ranges extend into the positive value range (Figure 20). In these periods, however, investigations of the distributions of accumulation and denudation in the DoD do not point to any processes that would explain an increase in sediment (Figure 19). A comparison of the trends without and with error weighting clearly shows that in both cases the linear trend reflects a decrease in the normalized balance and thus increased discharge. The annual discharge growth is 4,660 m³/a without error weighting and 1,440 m³/a with weighting. Therefore, the error weighting leads to a weakening of the negative balance trend. Both trendlines exhibit a poor fit with $R^2 = 0.03$ (Figure 20).

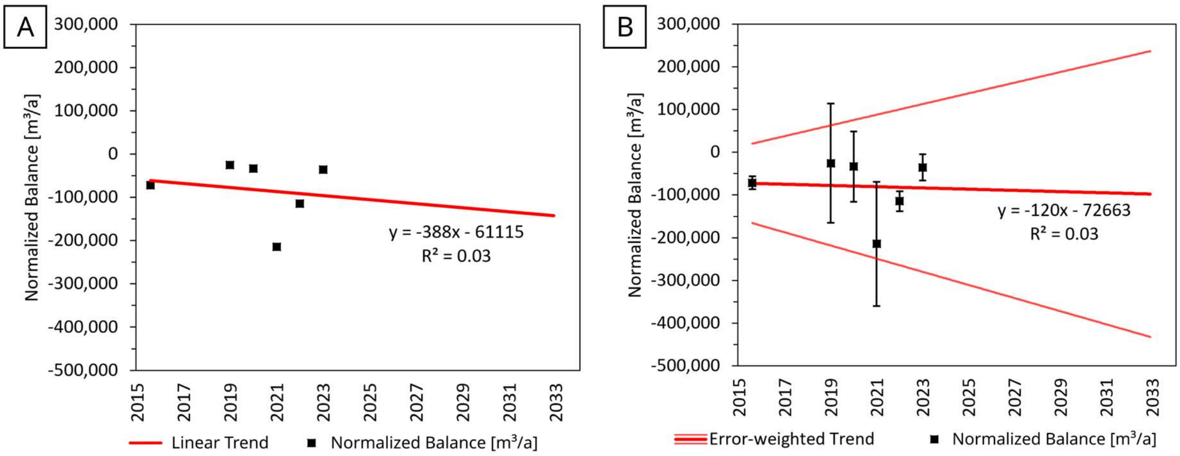

Figure 20: Trend of the error-corrected normalized balance of the slide based on data of 2012-2023 (a) without and (b) with error-weighting. Each equation depicts the linear trend with a monthly increase of x and $x_{08/2015}=1$.

5.3.3.3 Surface change of the debris cone

From 08/2012 to 09/2023, a total of approximately 540,000 m³ of sediment accumulated within the active debris cone, resulting in an average annual balanced rate of 39,000 m³/a and a mean elevation increase of 0.24 m/a (Table 9). All other analysed periods also show positive net change indicating a predominance of accumulation over denudation. A comparison between 08/2012-07/2018 and 07/2018-07/2023, alongside mean values from the annual analyses, reveals an increase in accumulated volumes in recent years. A lowering in the denudation leads to a higher normalized balance throughout the last years (Table 9, Table 10). Notably, the period from 07/2020 to 07/2021 exhibits the strongest sediment dynamics with extraordinary accumulation and denudation, accompanied by the highest net change (Table 10).

Table 9: Volumetric surface change of the debris cone including a pixel-based correction of the systematic error of DoDs covering mid-term analyses between 2012 and 2023.

Period	**Days of period**	**$V_{b, corr}$ [m³]**	**$V_{nd, corr}$ [m³/a]**	**$V_{na, corr}$ [m³/a]**	**$V_{nb, corr}$ [m³/a]**
22/08/2012 – 13/07/2018	2,151	135,088	14,435	46,312	22,923
13/07/2018 – 18/07/2023	1,831	220,808	7,997	59,763	44,017
22/08/2012 – 12/09/2023	4,038	428,603	7,952	49,133	38,742

$V_{b,corr}$ is the error-corrected volume of net change, $V_{nd,corr}$ of the annual denudation, $V_{na,corr}$ of the annual accumulation and $V_{nb,corr}$ of the annual net change.

Table 10: Volumetric surface change of the debris cone including a pixel-based correction of the systematic error of DoDs covering annual periods from July to July in 2018-2023.

Period	**Days of period**	**$V_{b, corr}$ [m³]**	**$V_{nd, corr}$ [m³/a]**	**$V_{na, corr}$ [m³/a]**	**$V_{nb, corr}$ [m³/a]**
13/07/2018 – 24/07/2019	376	9,179	5,124	19,064	8,910
24/07/2019 – 09/07/2020	351	34,261	16,393	23,540	35,628
09/07/2020 – 21/07/2021	377	62,972	65,942	138,733	60,968
21/07/2021 – 19/07/2022	363	43,313	24,816	72,599	43,552
19/07/2022 – 18/07/2023	364	34,969	4,016	57,697	35,065

$V_{b,corr}$ is the error-corrected volume of net change, $V_{nd,corr}$ of the annual denudation, $V_{na,corr}$ of the annual accumulation and $V_{nb,corr}$ of the annual net change.

As already mentioned before, the sediment dynamics in the debris cone are marked by sedimentary growth due to a positive normalized net change (Table 9, Table 10, Figure 21). Considering the error ranges in Figure 21, a dominating sediment discharge is also possible in the study intervals 2018-2021 due to high uncertainties.

A positive trend in the normalized balance is visible both without and with error weighting. Regardless of the uncertainties, the fit is $R^2 = 0.28$, whereas with weighting the accuracy increases to $R^2 = 0.48$. The gradient leads to a predicted average annual growth of the sediment cone of approximately 2,300 m³/a without and 2,980 m³/a with weighting. Accordingly, this results in an increased accumulation in the area of the debris cone (Figure 21).

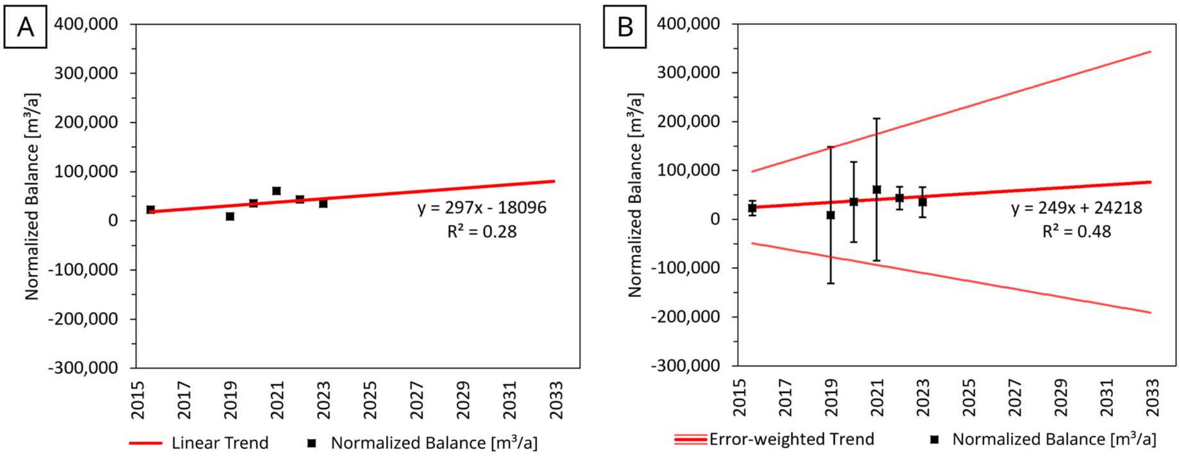

Figure 21: Trend of the error-corrected normalized balance of the debris cone based on data of 2012-2023 (a) without and (b) with error-weighting. Each equation depicts the linear trend with a monthly increase of x and $x_{08/2015}=1$.

5.4 Sediment exhaustion

The sediment exhaustion was analysed based on the error-weighted linear regression of the annual net change. The error-weighted trend was chosen due to a better coefficient of determination of the error-weighted linear regression in the debris cone compared to the linear trend without weighting and no change of the fit in the sliding area. Therefore, Figure 22 depicts the calculation predicted on an error-corrected linear trend of the balanced annual sediment discharge of the sliding area in the years 2012-2023. The 5 % error ranges refer to inaccuracies in the initial sediment volume determination of 01/2023. The annual values of sediment discharge and the remaining sediment volume for the error-corrected and non-corrected determination of exhaustion are attached in Appendix E and Appendix F, respectively.

The potential point of sediment exhaustion is determined between 2033 and 2042, assuming a linear sediment discharge based on the observed mean rates. In case of a reduced sliding area (Sc2) strong sedimentary discharge would end in 2033-2034. If no or a minor headscarp retreat occurs the sediment exhaustion time of scenarios 1, 3 and 4 would be reference points. Even though the differences in the initial sediment volume of these scenarios measure more than 250,000 m³, the sediment depletion time deviates from each other by only 17 months neglecting the error range. Considering the error margin, the depletion time reaches from 2035 to 2038. If the headscarp was to recede to the foot of the cirque back wall as in Sc5, sediment exhaustion can be expected between 2040 and 2042 (Figure 22).

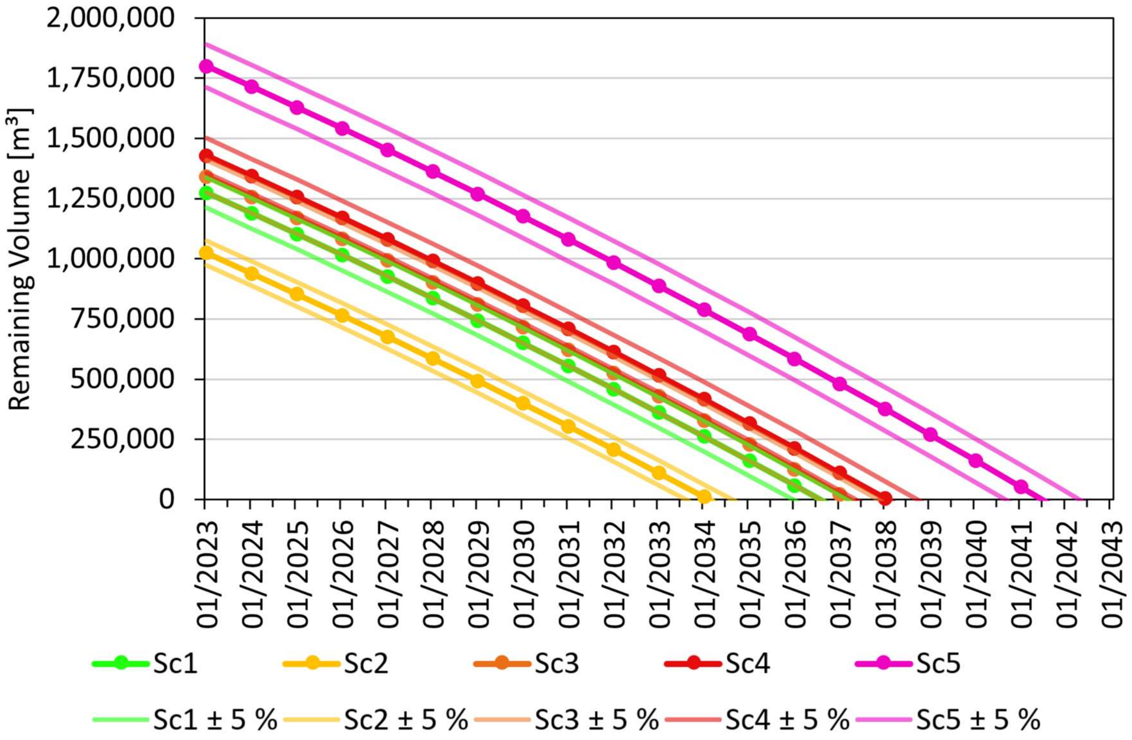

Figure 22: Sediment exhaustion of the Sattelkar, derived from an error-weighted linear increase in sediment discharge from the cirque. The linear trend is based on the error-corrected normalized balance of 08/2012-07/2023 and the uncertainties of each individual period.

6 Discussion

This study aims to estimate the sediment depletion time within the Sattelkar by quantifying the potentially mobilizable sediment volume and determining sediment dynamics. Bedrock interpolation and change detection using a time series of DEMs ranging from 2012 to 2023 revealed a sediment depletion time between 2033 and 2042. Geomorphologic processes and their dynamics within the entire study area are discussed based on the results of this work. Special focus lies on past and future developments as they are of high relevance for the determination of sediment depletion. Data quality is a key factor that significantly influences the results of the study and is therefore specifically evaluated. Finally, the relevance of the work and future action proposals are addressed.

6.1 Previous development

To be able to determine expected future changes, it is necessary to understand past process dynamics. As sediment dynamics are a central aspect of this work, the results are discussed in this chapter categorised by the data quality, short-term and long-term observations as well as a description of processes.

6.1.1 Data quality of surface changes

Although the DoD data is extremely useful for geomorphic monitoring, data uncertainties permit misinterpretation of elevation changes and the sediment budget. DEM deviance and propagated deviations from the actual vertical change in DoDs depend on data acquisition, data processing and topography (Wheaton et al. 2010). To quantify these inaccuracies, a determination of the mean deviance and inaccuracy of the error of the individual DoDs was carried out. Due to tilting and increased effects in steep terrain, Δz is not constant over the entire DoD, which is expressed in the uncertainties. Even though it must be noted that the chosen method with a manual sample selection of 15 height differences at fixed points also has a certain degree of inaccuracy, this approach enables an assessment of the reliability of the values.

The quantified z-deviations clearly show that generally strong vertical deviations and very high inaccuracies are present. DoDs that cover several years exhibit high systematic biases, however, by normalizing the volume changes of long periods to annual values the influence of errors is reduced. The periods 08/2012-07/2018, 07/2018-07/2023 and 08/2012-09/2023 therefore have a comparatively high accuracy (Table 4). In the case of the annual analyses from July to July, the error and uncertainties partially accounts for a multiple of the calculated change.

Based on the determined vertical displacements and inaccuracies, the LOD_{min} was set to 1 m for all DoDs. Except for a small area in the SW of the debris cone (Figure 19), errors could thus be extracted. A pixel-based correction of the accumulation and denudation volumes also increases the accuracy of the values $>LOD_{min}$. On the one hand, this procedure results in the loss of information from low-magnitude elevation changes below the LOD_{min} threshold, on the other hand, it enhances the geomorphological plausibility (Wheaton et al. 2010). Despite the consideration of error-corrected values in this work, the uncertainties and slight fluctuations should be taken into account.

For a more robust long-term assessment of sediment dynamics, annual net change trends were analyzed for both the slide and debris cone. Alongside a linear trend analysis, error-weighting was applied to enhance trend significance despite uncertainties. Notably, the determination coefficient increased substantially from $R^2 = 0.28$ to $R^2 = 0.48$ when considering uncertainties in the debris cone area, indicating a better fit with the error-weighted trend. Conversely, in the landslide area $R^2 = 0.03$ in both trends, suggesting no noticeable increase of significance despite differing gradients. Regarding the natural variability of the net changes due to various external influencing factors, an assessment beyond the physical categorisation of the deterministic relationship is necessary. Therefore, the correlation in the debris cone is seen as a reliable representation of recent trends, while caution is advised regarding the trend accuracy of the linear sediment discharge.

6.1.2 Short-term observations

When comparing the normalised volume changes in the cirque, significant fluctuations are evident in surface changes over shorter periods. Intra-annual variability can result in various effects on landslide intensity and surface sediment remobilization, despite similar annual precipitation totals. This is influenced by the intensity and timing of precipitation Winter precipitation, often in the form of snow from the previous year, can significantly affect thaw processes. Due to the generally high precipitation totals in July, the time of scanning in July is also crucial. With a minimally longer investigation period, more precipitation may occur during the survey time.

In both spatial and quantitative analyses, the years 2020-2022 stand out in terms of significant sediment changes in the landslide area. These are particularly evident in form of extensive denudation. The subsidence of the entire landslide body suggests that conditions at the sliding surface account for these changes. High pore water pressure leads to increased landslide activity (Carey et al. 2019). The analysis of precipitation and temperature conditions during this period further supports this inference. Air temperatures in 2020 and 2022, exceeding the long-term average, indicate potential thawing processes. Conversely, significant process activity in 2021 is attributable to a heavy precipitation event which occurred on 17/18 July 2021 (GeoSphere Austria 2023; GeoSphere Austria 2024b). The increased sediment dynamics of the period 07/2021-07/2022 and possibly also in 07/2020-07/2021 may have been caused by an elevated water availability at the sliding surface due to rapidly thawing snow or permafrost degradation.

6.1.3 Long-term observations

Surface changes over multiple years show smaller deviations than annual analyses, equalizing intra-annual and inter-annual variabilities. Long-term observations enable total discharge quantification, while shorter periods can identify trends in sediment dynamics.

The results of quantified sediment loss within the entire study area suggest that between 08/2012 and 09/2023 more than 430,000 m³ of sediment were removed by anthropogenic intervention or entered the lower reaches of the Obersulzbach through fluvial erosion. No statement can be made about the share of removed sediment by excavators (Kaindl 2014) after the large debris flows in the summer of 2014. In the comparison of the discharge of the periods 08/2012-07/2018 and 07/2018-07/2023, it becomes clear that the sediment input in the Obersulzbach has increased significantly in recent years. Since the sum of the values of 08/2012-07/2018 and 07/2018-07/2023 surpass the determined volume of 08/2012-09/2023 (Table 5) due to deviance uncertainties of the DEMs, the mid-term analyses of each period require scrutiny.

In the period 2012-2023, negative values indicate sediment discharge from the cirque, while positive balances in the debris cone denote sediment accumulation dominance. Currently, more sediment is excavated from the cirque than the debris cone accumulates. This can be derived from the comparison of the normalised balances of the sub-areas. Comparing the normalised net change of the cirque from 08/2012-09/2023 to that of the entire system, it becomes evident that around half of the sediment excavated from the cirque reaches the Obersulzbach without long intermediate storage.

In addition to the normalised balance quantification, the breakdown by accumulation and denudation reveals a trend. Both periods, 2012-2018 and 2012-2023, show lower accumulated and denudated values compared to annual changes and total differences from 2018-2023. This indicates a significant increase in sediment dynamics in recent years. The period 2012-2018 includes the sediment dynamics that led to the devastation of the Obersulzbach Valley in July 2014, yet dynamics are lower than in 2018-2023. This suggests that a calmer phase followed the excavation of more than 70,000 m³ from the cirque and considerable rearrangement processes in the debris cone area.

The analysis of the landslide and debris cone reveals that higher sediment dynamics from 2018 to 2023 can be attributed to notably variable and overall amplified denudation in the cirque. Conversely, the debris cone exhibits decreased denudation alongside increased accumulation. While both areas experience significant process intensity fluctuations, the variability in accumulation and denudation affects the debris cone balances minimally.

Plotting normalized net changes for the 2012-2018 period and annual investigations from 2018 to 2023 facilitates trend representation. The comparison of the quantified values of the mesoscale investigation periods 2012-2018 and 2018-2023 reveals increased sediment discharge from the cirque and accumulation on the debris cone (Figure 20, Figure 21). Concerning the sediment depletion model by Knight & Harrison (2018) (Figure 5), the landslide can be assigned to the initial stage with increasing sediment availability based on the linear trend. The activity model by Chen et al (2020) shows a continuous decrease in activity (Figure 6). The increasing discharge therefore deviates strongly from the model of Chen et al (2020), so that the landslide cannot be assigned to any of its stages. Therefore, the increasingly negative net change of the cirque suggests that, despite the exposure of increasingly large rock areas, depletion is unlikely to occur in the short future. A steeper balance gradient of the debris cone compared to the landslide indicates reduced sediment input into the Obersulzbach from the cirque discharge in recent years. Yet this is not reflected in the quantified data. While around 28,500 m^3/a of sediment was released during 2012-2018, sediment discharge increased fourfold to 2018-2023, reaching 114,500 m^3 annually. The discrepancy may be attributed to high sediment discharge from the cirque in 2020-2021, minimally influencing the normalized balance trend of the cirque due to inaccuracy. However, the debris cone trend, characterized by a higher determination coefficient ($R^2 = 0.48$), appears more reliable than the landslide trend. Thus, caution is warranted when using error-weighted trends to estimate future sediment discharge for depletion, which is discussed in more detail in Chapter 6.3.

6.1.4 Process description

The dynamics of the landslide processes exhibit notable patterns, evident in the discrepancies between short-term and long-term analyses, as well as in consecutive annual observations. Comparing normalized accumulation volumes from long-term analyses with annual periods reveals minimal long-term accumulation, attributed to the cyclical nature of process interactions. Material transported to the cirque threshold by rear landslides is subsequently expelled from the cirque via rockfalls or debris flows. Due to the nature of temporarily stored material in the accumulation zone, the duration since the last discharge event and its intensity are critical factors, preventing continuous material accumulation over time. Moreover, this cyclicality is evident in annual analyses, characterized by patterns of denudation and accumulation. Years with low accumulation are typically followed by periods of reduced erosion and vice versa, reflecting the recurrent discharge events.

Analyzing local positive and negative height differences provides insights into sediment processes in the debris cone area. The upper debris cone exhibits linear accumulation and denudation, with accumulation predominating in most years. Notably, in the period 07/2020-07/2021, pronounced linear deepening with height differences >5 m is evident, along with negative height differences in previously inactive areas. In the following year, intensive accumulation is observed in the NE areas of the debris cone, while erosion persists in the new channel, highlighting dynamic channel processes. Areal accumulation predominates in the active debris fan, except for 07/2019-07/2020, when areal denudation is visible (Figure 19). This, however, is attributable to DEM tilting and $\delta z = -0.78$ m ± 0.83 m exceeding LOD_{min} in this debris cone section. The combination of areal accumulation and linear erosion in the upper debris cone during 07/2020-07/2021 reflects typical debris flow patterns. In other annual investigation periods from 2018-2023, accumulation likely resulted from fluvial processes due to small areal extent.

6.2 Future development

Drawing from historical observations and geomorphological process analysis, this part addresses two main enquiries: (i) the variation in sediment volume across different landslide scenarios and (ii) the anticipated timeframe for sediment depletion in the Sattelkar. Therefore, the following section examines the plausibility of the five hypothesized scenarios based on field observations and temporal constraints regarding sediment depletion. These findings are further analyzed in terms of their influence on the accuracy of determined sediment depletion, considering both past and future factors influencing landslide and sediment dynamics.

6.2.1 Alteration of the landslide area

The mobilizable sediment volume was assessed across five scenarios, denoted as Sc1-5, representing potential changes within the landslide area. Scenarios Sc2 and Sc5 delineate the extremes, depicting the mobilization of the most active sediment areas in 2023 and of the entire sediment up to the cirque's headwall, respectively. The regressive movement of the headscarp in Sc5 spans 130-255 m. Sc1 corresponds to the current landslide area with a volume of around 1,246,000 m^3 in 09/2023 and 1,274,000 m^3 in 01/2023. Scenarios Sc3 and Sc4 depict observed shifts in the headscarp, with Sc3 showing an average offset of 15 m and locally up to 39 m southeast of the active landslide surface and the most recent backward displacement of the headscarp. In Sc4, the landslide surface extends towards the SSE direction, reaching up to 30 m beyond the terminal moraine and its lateral areas (Figure 15).

Due to the absence of comprehensive subsurface investigations, the influence of water-conducting layers or changes in sediment filling and strength on retrogressive trends cannot be determined. Nonetheless, scenario plausibility can be justified based on field investigations and orthophotos from 2018-2023. A comparison of headscarp positions between 07/2018 and 09/2023 reveals no retrogression at the northern edge. Conversely, significant activity is observed in the southeast, with extensive downslope mobilization, resulting in a total retreat of up to 55 m and an average retreat of 10.5 m/a. However, these movement rates are representative on a local scale but do not encompass the entire area. Lateral expansion of the landslide is minimal, reaching up to 18 m east of the terminal moraine, with isolated superficial cracks in the vegetation suggesting potential future remobilization. Overall, the landslide area increased by around 12,000 m² from 07/2018 to 09/2023. This corresponds to an annual increase of approximately 2,300 m².

Given the prognosis of depletion within 10.7-19.4 years from 01/2023, it is possible to estimate the volumetric increase and retrogressive headscarp retreat during this period, assuming consistent development. The volumetric increase is estimated to range from 14,600 m² to 44,620 m², with a potential retrogressive headscarp retreat of 112-204 m. It is essential to note that these calculations represent a maximum value, especially regarding length, as recent years have shown localized changes while other areas remain relatively stable.

The comparative analysis results suggest that under the same retrogressive development, the active landslide area is projected to increase to approximately 199,000 m² by August 2033 and up to around 229,000 m² by May 2042. The value slightly exceeds the area of Sc4 and surpasses that of Sc5 (Table 3). A moderate headscarp retreat of 112 m aligns with Sc5, while a retreat of 204 m exceeds the maximum distance to the cirque headwall. Given that Sc4 integrates the terminal moraine by lateral enlargement and Sc5 includes retrogressive landslides in formerly stable regions with retreats of up to 190 m, both scenarios deviate significantly from the anticipated development. A combined lateral and retrogressive surface expansion is more likely in terms of shape, which is approximately represented by Sc3. Consequently, Sc3, with an area of approximately 189,000 m², represents the expected development best with a slight headscarp regression in the forthcoming years. Additionally, a combination of Sc3 and Sc5, although not formally calculated, could be considered realistic. Despite current conditions suggesting an unlikely reduction in the landslide area analogue to Sc2 due to headscarp regression, recent minor movements in the southwest area of the landslide zone indicate potential stabilization in the future.

6.2.2 Mobilizable sediment volume

The accuracy of the sediment volume for each scenario is closely linked to bedrock interpolation. To determine sediment volume in the cirque, bedrock was initially interpolated using outcrops outside the sedimentary fill of the cirque floor and partially within the landslide area. However, no rock exposure exists in the centre of the Sattelkar, thus lacking punctual depth information. The interpolation was initially carried out along longitudinal and transverse profiles. These linear interpolations, coupled with area-wide elevation data, formed the foundation for generating a three-dimensional rock model of the cirque using "Topo To Raster". Subsequently, sediment thickness and volume for various scenarios were determined based on this model.

The used interpolation technique "Topo To Raster" is an acknowledged tool for generating hydrologically correct models, prevailing over other models when applied to glacial subsurface (Unger 2012). However, the accuracy of area-wide interpolation depends heavily on the quantity, distribution and quality of the input point or linear elevation data. While prioritizing geomorphologically plausible interpolation at intersection points of linear profiles helps mitigate discrepancies, uncertainties persist, particularly in areas with limited data quantification. In the centre of the landslide area, data quality is relatively high due to nearby rock outcrops. Nevertheless, in the central sediment fill volumetric deviations due to the interpolation have to be considered.

Comparable studies enable the evaluation of bedrock interpolation results. Urbini et al. (2017) note that cirque glaciers typically feature ridges and channels in their underlying bedrock, with the Sforzellina glacier exhibiting elevation differences of up to 15 meters, marked by gradual transitions. Moreover, Urbini et al. (2017) illustrate a distinction in bedrock morphology between cirque glaciers and larger counterparts with the latter displaying more pronounced subsurface structures. Grab et al. (2021) reinforce these observations for medium to large glaciers. Their analyses also indicate that the models GlaTE and ITVEO adequately depict the glacier bed, yet with some smoothing of actual structures (Grab et al. 2021). This must be considered for the glacier bed model HF used by Helfricht et al. (2019b), which exhibits an error margin of 25-31 %, particularly notable for small glaciers (Helfricht et al. 2019a). Nevertheless, modelled glacier bed elevation data by Helfricht et al. (2019b) and their model HF and rock surface data from recently deglaciated areas allow a comparison of the Sattelkar interpolation with other cirques in the Hohe Tauern region. Kleines Jaidbaichkees, Maurerkees, and Käferfeldkees are suitable comparative localities due to similar cirque structures, recent rock exposure and geological similarity. The longitudinal profiles of these cirques exhibit trough structures resulting from glacial erosion, with Käferfeldkees reveal a single depression below the recent glacier, while Kleines Jaidbachkees and Maurerkees are characterized by multiple overdeepenings and flattenings. A ridge and trough structure is also apparent in the transverse profile. While this is only slightly pronounced in the Maurerkees, the other cirques show height differences of up to 40 m and 45 m (Figure 23). Based on the observations, the interpolation results of the Sattelkar can therefore be considered realistic. However, it should be noted that the subsurface structures of the studied cirques have softer curves than in the interpolation (Figure 17, Figure 23). This is the case both for the presumably smoothed comparative interpolation and for the GPR data from Urbini et al (2017). Additionally, it is worth noting that the cirques with existing glaciers underwent longer glacial erosion, which is also included in the glacier bed model. This results in more pronounced hollow shapes compared to Sattelkar, which was deglaciated in the late glacial period (Otto et al. 2018). Consequently, basins in the interpolation may be exaggerated. Furthermore, the flattening below the cirque's back wall in the LP-STK-Central profile warrants scrutiny, as a gradual flattening continuation is more plausible (Figure 17, Figure 23). Strong edges in the subsurface model, influenced by linear interpolations, contribute to distinct structural features, potentially leading to local underestimations and overestimations of depth profiles. The underestimation in the LP-STK-Central profile over a length of 80-250 m and 400-580 m as well as an overestimation in the SW of the cirque must be emphasised. In summary, the quality of the interpolation in the area of the landslide can be rated as good due to the high point density in the model. The current landslide area (Sc2) and the future scenarios 3-5 only slightly extend into the presumably too shallow interpolated centre (Figure 15, Figure 18). It can therefore be assumed that the inaccuracies of the interpolation only have a minor influence on the volume. To account for errors, an additional error range of ± 5% was determined and applied to sediment depletion calculations.

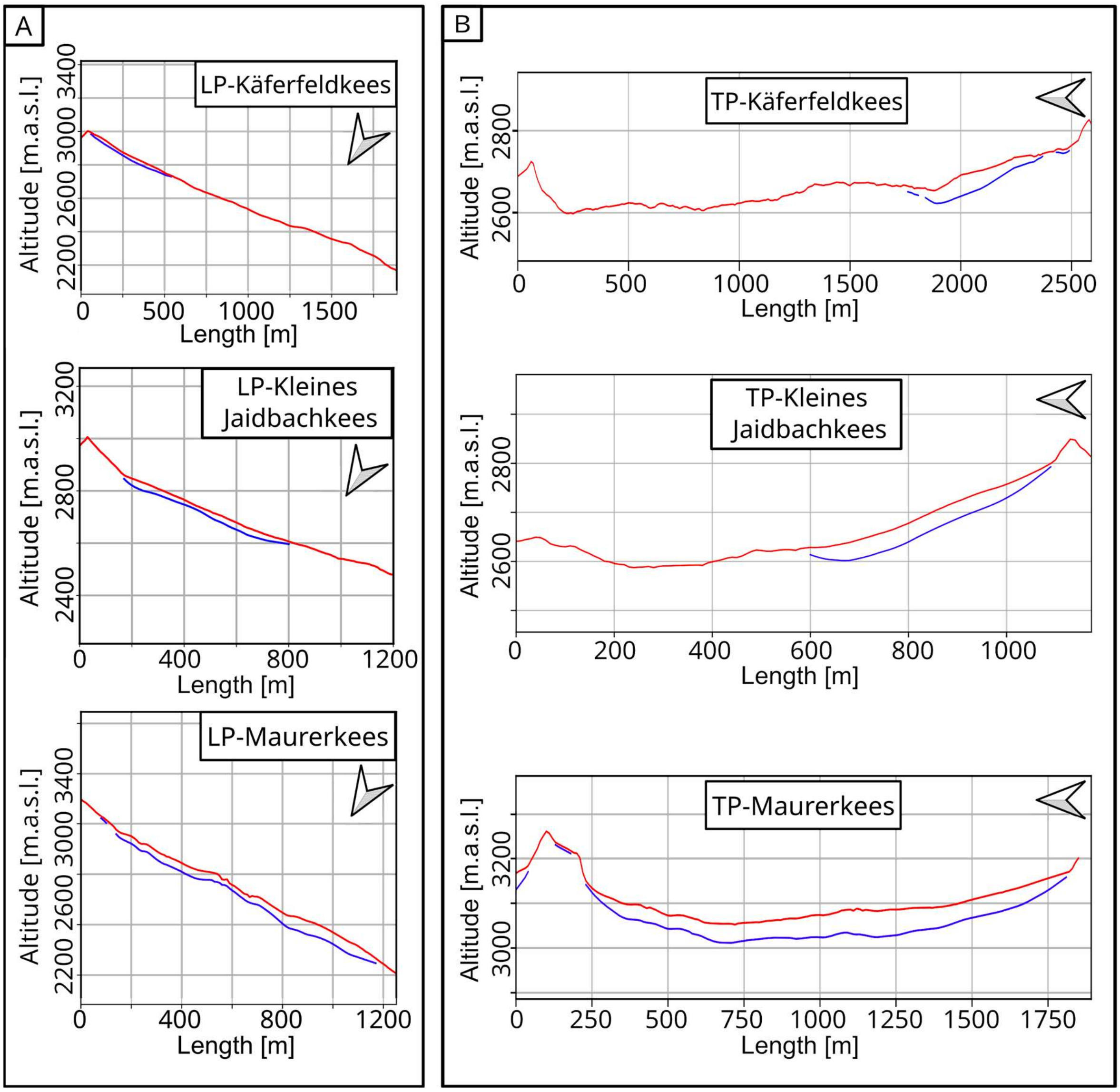

Figure 23: (a) Longitudinal and (b) transversal elevation profiles of comparable cirques to the Sattelkar showing the glacier bed interpolation (blue) and the surface derived from the DTM (red) (Data: Land Salzburg 2012; Helfricht et al. 2019b).

In addition to interpolation accuracy, the simplified calculation method may account for inaccuracies regarding sediment volumes. This method assumes that the sliding surface is positioned at the transition between bedrock and sediment filling. However, this simplification may not always reflect reality. For shallow landslides, it may lie within the sediment. Moreover, in case of a rotational landslide movement, the sliding surface exhibits a gradual flattening at the edges, contrary to the simplified assumption (Figure 24). Hence, while the simplified assumption may be reasonable in the northern and lower parts of the cirque, a gradient of the sliding surface towards the surface is more likely at the upper and southern boundaries. Consequently, the simplified calculation leads to a volumetric overestimation, although the extent of overestimation appears minimal, as drafted in Figure 24. Thus, it is likely that the lower uncertainty range of the initial sediment volume represents the closest approximation to reality.

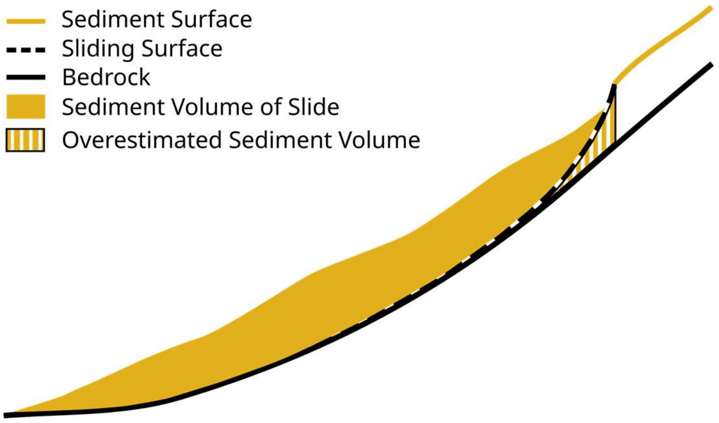

Figure 24: Schematic representation of the possibly overestimated sediment volume in a longitudinal section through the landslide. The overestimation is due to the simplified assumption that the interpolated bedrock over the entire landslide area corresponds to the sliding area.

6.2.3 Sediment exhaustion

The time of sediment depletion is influenced by various factors, whose future trajectories can be assumed but not predicted with certainty. As such, this timeframe should be viewed as a provisional estimate, subject to revision based on new research findings to enhance its reliability. However, the precision of the utilized values and influencing factors is debated. The discussion is based on the factors explained in Table 11, including the influence of inaccuracies of the sediment volume on the sediment depletion and the accuracy of the linear trend of the sediment discharge from the cirque due to natural fluctuations and climatic changes.

Table 11: Factors influencing the accuracy of sediment depletion time. "Overestimation" implies that the exhaustion time is prognosed too conservative, whereas in case of an "Underestimation" the factor leads to a later exhaustion. "No Change" means no significant variation. The size of the arrows displays the degree of uncertainty.

Overestimation ↑ No Change ~ Underestimation ↓

Sediment volume	Bedrock interpolation	↑ ~ ↓
	Simplified sliding surface	↑ ~
	Sliding area	↑ ~ ↓
Surface changes	Effect of inaccuracies on trend of normalised net change	↑
	Decrease in sediment availability as sediment depletion approaches	↑ ~ ↓
	Natural process variability	↑ ~ ↓
Climatic changes	Increase in variabilities	↑ ~ ↓
	Precipitation change	↑ ~ ↓
	Temperature change	↑ ~ ↓

As discussed in chapters 6.2.1 and 6.2.2, sediment volume significantly impacts depletion time. While the accuracy of is relatively good in areas with exposed rock, greater uncertainties exist in the southern landslide area and beyond. The simplified assumption that the bedrock corresponds to the sliding surface of the landslide over the entire area leads to a possibly slight overestimation of the volume. However, pronounced ridges at the southern edge mitigate this overestimation, especially for Sc4. Overall, the initial volume reduced by 5 % provides a good proxy for the other scenarios. Exhaustion time is strongly influenced based on the scenario and initial volume. Varying the integrated volume depending on headscarp retreat yields variations of nearly 9 years. Although a regression like Sc3 is assumable, precise statements await future observations.

The precision of sediment depletion data is influenced by the trend of sediment discharge from the cirque. Error-weighted linear regression, based on individual DoD error determinations, reduces the impact of systematic errors on sediment depletion. However, this method may underestimate the influence of high discharge periods, such as in 07/2020-07/2021, on the exhaustion estimation. The suitability of error-weighted linear regression versus a linear trend excluding uncertainties is debatable. Latter usage would lead to a significant deviance with an earlier depletion of 2.5-5.0 years (Appendix E, Appendix F).

Changes in sediment availability can either prolong or shorten depletion time. Reduced landslide dynamics with lower sediment availability may underestimate depletion time, while increased rock exposure can slow down landslides by reducing sediment load. However, thinner sediment layers facilitate infiltration, leading to mobilization with lower precipitation.

Considering the significant variability in normalized net change, the accuracy of a linear trend in reflecting reality is debatable. Variations in sediment discharge and landslide dynamics, as seen during the study period, have a substantial impact. As the analysis of 2012-2018 clearly shows, large sediment discharges are equalized over time by subsequent low sediment availability. However, individual events such as in 2014 could significantly alter conditions and advance depletion. Although events like the 2014 discharge of around 70,000 m^3 (Anker et al. 2016), which falls within the observed annual discharge of recent years, have a minor effect on timing, extreme events could lead to significant depletion advancements.

Meteorological factors contribute significantly to variabilities in sediment discharge. Discharge is closely linked to sediment availability, governed by landslide dynamics and processes like debris flows and rockfall, necessitating separate consideration. According to Hermle et al. (2022), the Sattelkar landslide aligns with a slow-moving deep-seated landslide. Thus, its dynamics rely on seasonal precipitation and substrate saturation levels, while increased short-term precipitation mobilizes debris flows. The impact of climate change on landslides remains unclear, given the mixed influences of temperature and precipitation (Gariano and Guzzetti 2016). Temperature data suggest sporadic permafrost presence (Keuschnig et al. 2021), yet its current effect on slope stability is ambiguous. Therefore, the effect of a future increase in temperature on permafrost degradation and thus slope stability, as seen in recent years (Figure 9), remains uncertain. For landslide dynamics and debris flows variability also plays a major role (Gariano and Guzzetti 2016). These effects even outweigh long-term climatic trends as sediment depletion falls into shorter time periods. Thus, assumptions about climate change impacts on sediment discharge are difficult to state. However, the net change trend over 11 years already incorporates variability.

In summary, numerous unpredictable and unquantifiable factors account for the high level of uncertainty in predicting sediment depletion time resulting in both overestimation and underestimation. While uncertainties in DoDs and volume calculation tend to lead to a conservative estimate, their impact is relatively low given the overall uncertainty level.

6.3 Implications for hazard assessment

The findings obtained in this work can be used for hazard assessment and preventive risk reduction measures. This section therefore addresses the relevance of the sediment depletion results and the trends in the net change of the landslide and debris cone for the planning of mitigation strategies and proposes actions.

This study provides estimates of expected mobilizable sediment volumes within the Sattelkar and their depletion time. Potential inaccuracies, highlight the need for further investigations to improve precision. Uncertainties in sediment volume estimation stem largely from the uncertain future development within the landslide area. However, ongoing monitoring enables containment of the potential landslide area based on forthcoming developments. Future studies on sediment discharge and landslide movement will help to understand further sediment dynamics in the cirque and to enable a re-evaluation of this study’s results. Special attention should be given to sediment availability near the cirque threshold. In case of high sediment availability and expected heavy precipitation, warnings can be issued at short notice. Continued monitoring is therefore essential for the precise assessment of the hazard potential.

To ensure the reliability of sediment depletion assessments and hazard mitigation planning, optimized alignment of DSM point clouds is required. Tilt-induced inaccuracies, sometimes surpassing annual volume changes, hinder the precise determination of sediment depletion time and prediction of sediment input into the Obersulzbach. This input is crucial for assessing bedload potential and planning measures downstream. Comparing net change trends in landslide and debris cone contributes to the prognostication of the input volume and its proportion to cirque discharge. However, results vary significantly depending on the use of error-weighted or unweighted landslide trends, necessitating DSM revision. Anker et al. (2016) stress the need for adjustment to changing conditions in the catchment area of the Obersulzbach with a bedload retention system. The existing torrent controls in the lower reaches are filled crown barriers, which only regulate the velocity of the Obersulzbach, but lack sediment retention capability. Hence, plans for a consolidation barrier upstream of the Blausee dams with an estimated capacity of 150,000-200,000 m^3 exist (Anker et al. 2016). Considering the current input ratio, full discharge of the 1,000,000-1,800,000 m^3 landslide may surpass the sediment capacity of the panned basin, even with intermediate storage in the middle reaches of the Obersulzbach. Continuous analysis with revised data and incorporation of new developments are therefore highly relevant.

7 Conclusion

This research study examined sediment availability, dynamics and exhaustion time within an active landslide in the Sattelkar cirque. To answer these research questions an interpolation of the sub-surface bedrock of the cirque, a change detection analysis between 8 DEMs ranging from 2012-2023 and an extrapolation of the linear trends of this timeframe was carried out. The results revealed significant variability in sediment volumes across different sliding scenarios, ranging from approximately 1,000,000 m^3 to 1,800,000 m^3. Based on the current headscarp retreat, scenario Sc3 depicts the most realistic future sliding area with an initial sediment volume of 1,341,739 ± 67,087 m^3 for determining sediment exhaustion. Observations of sediment dynamics between 08/2012 and 07/2023 highlighted an increasing sediment discharge from the sliding area alongside a progressive accumulation in the debris cone. Regarding the prognosis for sediment exhaustion within the active slide, the study estimates a timeframe between 2033 and 2042. However, uncertainties in sediment volume quantification and unpredictable trajectories of influencing factors underscore the possibility of over- or underestimating the time of sediment exhaustion.

Therefore, further investigations are necessary to evaluate the applied methodology and reduce uncertainties through the acquisition of additional data and revision of existing data. Continuous monitoring of the study area, with focus on sliding area alterations and sediment availability near the threshold, as well as improving georeferencing accuracy of DSMs is suggested. To gain deeper insights into bedrock geometry and erosion patterns of cirque glaciers, conducting geophysical surveys of the sub-surface is recommended.

The research provides valuable insights into sediment dynamics and exhaustion within active landslides, filling gaps in the existing sparse data, and serves as a reference point for hazard analyses. Although a generalization is limited by the complexity of landslides, the gained knowledge permits an enhanced transferability of the expected sediment dynamics to similar slow-moving landslides. Furthermore, it helps to understand sediment dynamics of landslides on a wider scale.

References

Anker, F., Fegerl, L., Hübl, J., Neumayer, F., Keuschnig, M. and Kaitna, R. (2016). Geschiebetransport in Gletscherbächen der Hohen Tauern: Beispiel Obersulzbach. In: Markus Moser/Florian Rudolf-Miklau (Eds.). Feststofftransport und Sedimentmanagement, 86–96.

Ballantyne, C. K. (2002). Paraglacial geomorphology. Quaternary Science Reviews 21 (18-19), 1935–2017. https://doi.org/10.1016/S0277-3791(02)00005-7.

Ballantyne, C. K. (2003). Paraglacial landform succession and sediment storage in deglaciated mountain valleys: theory and approaches to calibration. Zeitschrift für Geomorphologie 132, 1–18.

Ballantyne, C. K. and Benn, D. I. (1994). Paraglacial Slope Adjustment and Resedimentation Following Recent Glacier Retreat, Fabergstolsdalen, Norway. Arctic and Alpine Research 26 (3), 255. https://doi.org/10.2307/1551938.

Benn, D. I. and Evans, D. J. A. (2010). Glaciers & glaciation. 2nd ed. London, Hodder Education.

Blöthe, J. H. and Korup, O. (2013). Millennial lag times in the Himalayan sediment routing system. Earth and Planetary Science Letters 382, 38–46. https://doi.org/10.1016/j.epsl.2013.08.044.

Bundesamt für Eich- und Vermessungswesen (BEV) (2021). Verwaltungsgrenzen (VGD) - Stichtagsdaten grundstücksgenau. URL: https://www.data.gv.at/katalog/dataset/51bdc6dc-25ae-41de-b8f3-938f9056af62#resources.

Bundesministerium Land- und Forstwirtschaft, Regionen und Wasserwirtschaft (BML) (2023). eHYD. Der Zugang zu hydrographischen Daten Österreichs. URL: https://ehyd.gv.at/?g_suche=203034.

Carey, J. M., Massey, C. I., Lyndsell, B. and Petley, D. N. (2019). Displacement mechanisms of slow-moving landslides in response to changes in porewater pressure and dynamic stress. Earth Surface Dynamics 7 (3), 707–722. https://doi.org/10.5194/esurf-7-707-2019.

Chen, M., Tang, C., Xiong, J., Shi, Q. Y., Li, N., Gong, L. F., Wang, X. D. and Tie, Y. (2020). The long-term evolution of landslide activity near the epicentral area of the 2008 Wenchuan earthquake in China. Geomorphology 367, 107317. https://doi.org/10.1016/j.geomorph.2020.107317.

Church, M. and Ryder, J. (1972). Paraglacial Sedimentation: A Consideration of Fluvial Processes Conditioned by Glaciation. Geological Society of America (92), 3059–3071. https://doi.org/10.1130/0016-7606(1972)83[3059:PSACOF]2.0.CO;2.

Church, M. and Slaymaker, O. (1989). Disequilibrium of Holocene sediment yield in glaciated British Columbia. Nature 337 (6206), 452–454. https://doi.org/10.1038/337452a0.

Cossart, E. and Fort, M. (2008). Sediment release and storage in early deglaciated areas: Towards an application of the exhaustion model from the case of Massif des Écrins (French Alps) since the Little Ice Age. Norsk Geografisk Tidsskrift - Norwegian Journal of Geography 62 (2), 115–131. https://doi.org/10.1080/00291950802095145.

Damm, B. and Felderer, A. (2013). Impact of atmospheric warming on permafrost degradation and debris flow initiation: A case study from the eastern European Alps. E&G Quaternary Science Journal 62 (2), 136–149. https://doi.org/10.3285/eg.62.2.05.

Dietrich, A. and Krautblatter, M. (2017). Evidence for enhanced debris-flow activity in the Northern Calcareous Alps since the 1980s (Plansee, Austria). Geomorphology 287, 144–158. https://doi.org/10.1016/j.geomorph.2016.01.013.

EfrainMaps (2020). Europe Countries. URL: https://www.efrainmaps.es/english-version/free-downloads/europe/.

Evans, I. S. (2009). Allometric development of glacial cirques: an application of specific geomorphometry. In: Purves, R.S., Gruber, S., Straumann, R.K., Hengl, T. (Ed.). Proceedigs of Geomorphometry 2019, Zurich, 31.08.2019-02.09.2019, 248–253.

Evans, I. S. and Cox, N. J. (1974). Geomorphometry of the Operational Definition of Cirques. Area 6, 150–153.

Gariano, S. L. and Guzzetti, F. (2016). Landslides in a changing climate. Earth-Science Reviews 162, 227–252. https://doi.org/10.1016/j.earscirev.2016.08.011.

geoland.at. Geoland Basemap Gelände. URL: https://mapsneu.wien.gv.at/basemapneu/1.0.0/WMTSCapabilities.xml.

GeoSphere Austria (2023). Jahrbuch. URL: https://www.zamg.ac.at/cms/de/klima/klimaueber-sichten/jahrbuch.

GeoSphere Austria (2024a). Automatisch Wetterstation "Rudolfshütte". URL: https://www.zamg.ac.at/gemwetter/rudolfshuette/rudolfshuette.htm.

GeoSphere Austria (2024b). Messstationen Stundendaten. GeoSphere Austria. URL: https://data.hub.geosphere.at/dataset/klima-v1-1h.

Grab, M., Mattea, E., Bauder, A., Huss, M., Rabenstein, L., Hodel, E., Linsbauer, A., Langhammer, L., Schmid, L., Church, G., Hellmann, S., Délèze, K., Schaer, P., Lathion, P., Farinotti, D. and Maurer, H. (2021). Ice thickness distribution of all Swiss glaciers based on extended ground-penetrating radar data and glaciological modeling. Journal of Glaciology 67 (266), 1074–1092. https://doi.org/10.1017/jog.2021.55.

Hartmeyer, I., Keuschnig, M., Delleske, R., Krautblatter, M., Lang, A., Schrott, L., Prasicek, G. and Otto, J.-C. (2020). A 6-year lidar survey reveals enhanced rockwall retreat and modified rockfall magnitudes/frequencies in deglaciating cirques. Earth Surface Dynamics 8 (3), 753–768. https://doi.org/10.5194/esurf-8-753-2020.

Haynes, V. M. (1968). The Influence of Glacial Erosion and Rock Structure on Corries in Scotland. Geografiska Annaler: Series A, Physical Geography 50 (4), 221. https://doi.org/10.2307/520780.

Helfricht, K., Huss, M., Fischer, A. and Otto, J.-C. (2019a). Calibrated Ice Thickness Estimate for All Glaciers in Austria. Frontiers in Earth Science 7. https://doi.org/10.3389/feart.2019.00068.

Helfricht, K., Huss, M., Fischer, A. and Otto, J.-C. (2019b). Spatial ice thickness distribution and glacier bed elevation for glaciers of the third Austrian Glacier Inventory (GI3). https://doi.org/10.1594/PANGAEA.898651.

Hermle, D., Gaeta, M., Krautblatter, M., Mazzanti, P. and Keuschnig, M. (2022). Performance Testing of Optical Flow Time Series Analyses Based on a Fast, High-Alpine Landslide. Remote Sensing 14 (3), 455. https://doi.org/10.3390/rs14030455.

Hermle, D., Keuschnig, M., Hartmeyer, I., Delleske, R. and Krautblatter, M. (2021). Timely prediction potential of landslide early warning systems with multispectral remote sensing:

a conceptual approach tested in the Sattelkar, Austria. Natural Hazards and Earth System Sciences 21 (9), 2753–2772. https://doi.org/10.5194/nhess-21-2753-2021.

Hinderer, M. (2001). Late Quaternary denudation of the Alps, valley and lake fillings and modern river loads. Geodinamica Acta 14 (4), 231–263. https://doi.org/10.1080/09853111.2001.11432446.

Hoffmann, T. (2015). Sediment residence time and connectivity in non-equilibrium and transient geomorphic systems. Earth-Science Reviews 150, 609–627. https://doi.org/10.1016/j.earscirev.2015.07.008.

Hoffmann, T., Müller, T., Johnson, E. A. and Martin, Y. E. (2013). Postglacial adjustment of steep, low-order drainage basins, Canadian Rocky Mountains. Journal of Geophysical Research: Earth Surface 118 (4), 2568–2584. https://doi.org/10.1002/2013JF002846.

Hovius, N., Stark, C. P. and Allen, P. A. (1997). Sediment flux from a mountain belt derived by landslide mapping. Geology 25 (3), 231. https://doi.org/10.1130/0091-7613(1997)025<0231:SFFAMB>2.3.CO;2.

Jin, S., Li, Z., Wang, Z., Wang, F., Xu, C. and Ai, S. (2020). Ice thickness distribution and volume estimation of Burqin Glacier No. 18 in the Chinese Altay Mountains. Journal of Arid Land 12 (6), 905–916. https://doi.org/10.1007/s40333-020-0083-9.

Kaindl, A. (2014). 15 Meter hohe Mure verperrt Tal. Die Unwetter haben einTal im Oberpinzgau komplett verändert. Zehn Bagger graben den Weg zu den Almen frei und zwingen den Bach wieder in ein Bett. Salzburger Nachrichten of 2014, 4–5. URL: https://www.pressreader.com/austria/salzburger-nachrichten/20140811.

Karl, F. and Schmidegg, O. (1979). 151 Krimml. Blatt 3706. Wien, Geologische Bundesanstalt. URL: https://opac.geologie.ac.at/wwwopacx/wwwopac.ashx?command=getcontent&server=images&value=GK0151_000_A.pdf.

Keuschnig, M., Delleske, R. and Hartmeyer, I. (2021). Klimasensitive, hochalpine Kare: Projekt Sattelkar. Endbericht 2021. URL: http://www.parcs.at/nphts/pdf_public/2022/50889_20220705_124435_Endbericht_Sattelkar_2021.pdf.

Knight, J. and Harrison, S. (2018). Transience in cascading paraglacial systems. Land Degradation & Development 29 (6), 1991–2001. https://doi.org/10.1002/ldr.2994.

Köppen, W. (1936). Das geographische System der Klimate. In: Wladimir Köppen/Rudolf Geiger (Eds.). Handbuch der Klimatologie.

Land Salzburg (2023a). Gewässer-Einzugsgebiete Land Salzburg. URL: https://www.data.gv.at/katalog/dataset/3ccfbe49-782d-4bb1-9b3d-f38e45b44079#resources.

Land Salzburg (2023b). Gewässernetz Land Salzburg. URL: https://www.data.gv.at/katalog/dataset/ea68ecc1-b0bb-4911-ad81-fe6e0112a0ed#additional-info.

Land Salzburg (2023). SAGISonline. URL: https://www.salzburg.gv.at/sagismobile/sagisonline.

Land Salzburg (Hrsg.) (2012). 50614 Neukirchen am Großvenediger. DGM 1m(tif) 2012. URL: https://www.salzburg.gv.at/sagisdaten_download/SAGIS_DATEN/ALS/50614_DGM_tif.zip.

Lewis, W. V. (Ed.) (1960). Norwegian Cirque Glaciers. London, Royal Geographical Society and John Murray.

Lieb, G. K., Kellerer-Pirklbauer, A. and Kleinferchner, H. (2012). Second rock glacier inventory (RGI2) of Central and Eastern Austria, link to Shapefile. https://doi.org/10.1594/PANGAEA.869805.

Mercier, D. (2008). Paraglacial and paraperiglacial landsystems: concepts, temporal scales and spatial distribution. Géomorphologie: relief, processus, environnement 4, 223–234. URL: https://journals.openedition.org/geomorphologie/7396?file=1.

MeteoNews AG (2024). Klima Rudolfshütte. Temperatur, Niederschlag. URL: https://meteonews.at/de/Klima/M11138000/Rudolfsh%C3%BCtte.

Olefs, M., Formayer, H., Gobiet, A., Marke, T., Schöner, W. and Revesz, M. (2021). Past and future changes of the Austrian climate – Importance for tourism. Journal of Outdoor Recreation and Tourism 34, 100395. https://doi.org/10.1016/j.jort.2021.100395.

Otto, J.-C. (2006). Paraglacial sediment storage quantification in the Turtmann Valley, Swiss Alps. Dissertation. Bonn, Rheinischen Friedrich-Wilhelms-Universität Bonn; Rheinische Friedrich-Wilhelms-Universität Bonn.

Otto, J.-C., Keuschnig, M. and Hartmeyer, I. (2018). Naturgefahren in alpinen Permafrostregionen und Permafrostmonitoring. Geographische Rundschau (11), 30–35.

Otto, J.-C., Schrott, L. and Keller, F. (2020). Map of permafrost distribution for Austria, Europe. https://doi.org/10.1594/PANGAEA.917719.

Otto, J.-C., Schrott, L., Jaboyedoff, M. and Dikau, R. (2009). Quantifying sediment storage in a high alpine valley (Turtmanntal, Switzerland). Earth Surface Processes and Landforms 34 (13), 1726–1742. https://doi.org/10.1002/esp.1856.

Paasche, Ø. (2011). Cirque Glaciers. In: Vijay P. Singh/Pratap Singh/Umesh K. Haritashya (Eds.). Encyclopedia of snow, ice and glaciers. Dordrecht, Springer, 141–144.

Pedraza, J., Carrasco, R. M., Villa, J., Soteres, R. L., Karampaglidis, T. and Fernández-Lozano, J. (2019). Cirques in the Sierra de Guadarrama and7 Somosierra Mountains (Iberian Central System): Shape, size and controlling factors. Geomorphology 341, 153–168. https://doi.org/10.1016/j.geomorph.2019.05.024.

Sanders, J. W., Cuffey, K. M., MacGregor, K. R. and Collins, B. D. (2013). The sediment budget of an alpine cirque. Geological Society of America Bulletin 125 (1-2), 229–248. https://doi.org/10.1130/B30688.1.

Sanders, J. W., Cuffey, K. M., MacGregor, K. R., Kavanaugh, J. L. and Dow, C. F. (2018). Variations in the surface velocity of an alpine cirque glacier. Journal of Glaciology 64 (248), 969–976. https://doi.org/10.1017/jog.2018.85.

Savi, S., Comiti, F. and Strecker, M. R. (2021). Pronounced increase in slope instability linked to global warming: A case study from the eastern European Alps. Earth Surface Processes and Landforms 46 (7), 1328–1347. https://doi.org/10.1002/esp.5100.

Schoch-Baumann, A. F. (2022). Sediment storage in the Upper Rhone Valley, Switzerland. Dissertation. Bonn, Rheinischen Friedrich-Wilhelms-Universität Bonn.

Schrott, L. and Adams, T. (2002). Quantifying sediment storage and Holocene denudation in an Alpine basin, Dolomites, Italy. Zeitschrift für Geomorphologie N.F. Suppl.-Bd. 128, 129–145.

Schrott, L., Otto, J.-C., Keller, F. and Rosner, M.-L. (2012). Permafrost in den Hohen Tauern. Abschlussbericht. geomorphology.at. URL: https://www.parcs.at/npht/pdf_public/2020/40358_20200915_135643_Abschlussbericht-Permalp-Final_verkleinert.pdf.

Stroeven, A. P., Harbor, J. and Heyman, J. (2013). Erosional Landscapes. In: John F. Shroder/R. Giardino (Eds.). Glacial and Periglacial Geomorphology. San Diego, Academic Press, 100–112.

Urbini, S., Zirizzotti, A., Baskaradas, J., Tabacco, I., Cafarella, L., Senese, A., Smiraglia, C. and Diolaiuti, G. (2017). Airborne Radio Echo Sounding (RES) measures on Alpine Glaciers to evaluate ice thickness and bedrock geometry: preliminary results from pilot tests performed in the Ortles Cevedale Group (Italian Alps). Annals of Geophysics 60 (2). https://doi.org/10.4401/ag-7122.

Vorkauf, M., Marty, C., Kahmen, A. and Hiltbrunner, E. (2021). Past and future snowmelt trends in the Swiss Alps: the role of temperature and snowpack. Climatic Change 165 (3). https://doi.org/10.1007/s10584-021-03027-x.

Wheaton, J. M., Brasington, J., Darby, S. E. and Sear, D. A. (2010). Accounting for uncertainty in DEMs from repeat topographic surveys: improved sediment budgets. Earth Surface Processes and Landforms 35 (2), 136–156. https://doi.org/10.1002/esp.1886.

Williams, R. D. (2012). DEMs of Difference. Geomorphological Techniques 2 (3.2), 1–17. URL: https://eprints.gla.ac.uk/114527/1/Williams%202012%20DEMs%20of%20Difference.pdf.

Zangerl, C., Prager, C., Brandner, R., Brückl, E., Eder, S., Fellin, W., Tentschert, E., Poscher, G. and Schönlaub, H. (2008). Methodischer Leidfaden zur prozessorientierten Bearbeitung von Massenbewegungen. Mit 38 Abbildungen. Geo.Alp 5, 1–51. URL: https://www2.uibk.ac.at/downloads/c715/geoalp_5_08/01zangerl_et_al_sml.pdf.

Zhang, T., Li, D., Kettner, A. J., Zhou, Y. and Lu, X. (2021). Constraining Dynamic Sediment-Discharge Relationships in Cold Environments: The Sediment-Availability-Transport (SAT) Model. Water Resources Research 57 (10). https://doi.org/10.1029/2021WR030690.

Appendix

List of appendix

Appendix A: Error-corrected and uncorrected volumetric change of the combined area of the Sattelkar landslide and debris cone.

Period	07/2018-07/2019	07/2019-07/2020	07/2020-07/2021	07/2021-07/2022	07/2022-07/2023	07/2018-07/2023	08/2012-09/2023	08/2012-07/2018
Days	376	351	377	363	364	1,831	4,038	2,151
Area [m^2]	346,660	346,660	346,660	346,660	346,660	346,660	350,508	306,035
V_b [m^3]	-78,489	-48,237	-113,404	-81,349	7,988	-606,395	-436,740	-45,267
V_d [m^3]	118,162	101,537	304,690	180,698	87,006	656,437	1,024,042	410,932
V_a [m^3]	39,673	53,300	191,287	99,349	94,994	348,598	587,302	365,666
$V_{b,\,corr}$ [m^3]	-78,489	-48,237	-113,404	-81,349	7,988	-606,395	-436,740	-45,267
$V_{d,\,corr}$ [m^3]	118,162	101,537	304,690	180,698	87,006	656,437	1,024,042	410,932
$V_{a,corr}$ [m^3]	39,673	53,300	191,287	99,349	94,994	348,598	587,302	365,666
$V_{nd,\,corr}$ [m^3/a]	114,705	105,587	294,992	181,694	87,245	130,857	92,564	69,731
$V_{na,\,corr}$ [m^3/a]	38,513	55,426	185,198	99,896	95,255	69,491	53,087	62,049
$V_{nb,\,corr}$ [m^3/a]	-76,192	-50,161	-109,794	-81,797	8,010	-120,882	-39,477	-7,681

V_b is the volume of net change, V_d of the denudation and V_a of the accumulation; $V_{b,corr}$, $V_{d,corr}$ and $V_{a,corr}$ are the error corrected volumes of net change, denudation and accumulation; $V_{nd,corr}$, $V_{na,corr}$ and $V_{nb,corr}$ are the error-corrected annual volume changes.

Appendix B: Error-corrected and uncorrected volumetric change of the Sattelkar landslide.

Period	07/2018-07/2019	07/2019-07/2020	07/2020-07/2021	07/2021-07/2022	07/2022-07/2023	07/2018-07/2023	08/2012-09/2023	08/2012-07/2018
Days	376	351	377	363	364	1,831	4,038	2,151
Area [m^2]	185,756	185,756	185,756	185,756	185,756	185,756	185,756	176,026
V_b [m^3]	-98,030	-27,723	-200,800	-133,078	-64,111	-606,395	-919,300	-285,892
V_d [m^3]	113,386	64,558	238,826	156,919	83,602	619,641	940,504	335,482
V_a [m^3]	15,356	36,835	38,026	23,841	19,490	13,246	21,204	49,590
$V_{b,\,corr}$ [m^3]	-26,332	-32,218	-221,608	-113,758	-35,434	-478,790	-919,300	-421,503
$V_{d,\,corr}$ [m^3]	81,389	66,011	247,402	148,491	71,766	558,583	940,504	389,502
$V_{a,corr}$ [m^3]	19,208	36,040	36,198	25,073	21,994	15,990	21,204	35,804
$V_{nd,\,corr}$ [m^3/a]	79,008	68,643	239,527	149,309	71,963	111,350	85,013	66,094
$V_{na,\,corr}$ [m^3/a]	18,646	37,478	35,045	25,211	22,054	3,188	1,917	6,075
$V_{nb,\,corr}$ [m^3/a]	-25,562	-33,503	-214,554	-114,385	-35,531	-95,444	-83,097	-71,524

V_b is the volume of net change, V_d of the denudation and V_a of the accumulation; $V_{b,corr}$, $V_{d,corr}$ and $V_{a,corr}$ are the error corrected volumes of net change, denudation and accumulation; $V_{nd,corr}$, $V_{na,corr}$ and $V_{nb,corr}$ are the error-corrected annual volume changes.

Appendix C: Error-corrected and uncorrected volumetric change of the Sattelkar debris cone.

Period	07/2018-07/2019	07/2019-07/2020	07/2020-07/2021	07/2021-07/2022	07/2022-07/2023	07/2018-07/2023	08/2012-09/2023	08/2012-07/2018
Days	376	351	377	363	364	1,831	4,038	2,151
Area [m^2]	160,904	160,904	160,904	160,904	160,904	160,904	164,906	130,053
V_b [m^3]	19,541	-20,515	87,395	51,729	72,100	298,556	482,560	240,626
V_d [m^3]	4,776	36,979	65,864	23,779	3,404	36,796	83,538	75,450
V_a [m^3]	24,318	16,465	153,259	75,508	75,504	335,352	566,098	316,076
$V_{b, corr}$ [m^3]	9,179	34,261	62,972	43,313	34,969	220,808	428,603	135,088
$V_{d, corr}$ [m^3]	5,278	15,764	68,110	24,680	4,005	40,117	87,976	85,067
$V_{a,corr}$ [m^3]	19,638	22,638	143,294	72,201	57,539	299,799	543,558	272,924
$V_{nd, corr}$ [m^3/a]	5,124	16,393	65,942	24,816	4,016	7,997	7,952	14,435
$V_{na, corr}$ [m^3/a]	19,064	23,540	138,733	72,599	57,697	59,763	49,133	46,312
$V_{nb, corr}$ [m^3/a]	8,910	35,628	60,968	43,552	35,065	44,017	38,742	22,923

V_b is the volume of net change, V_d of the denudation and V_a of the accumulation; $V_{b,corr}$, $V_{d,corr}$ and $V_{a,corr}$ are the error corrected volumes of net change, denudation and accumulation; $V_{nd,corr}$, $V_{na,corr}$ and $V_{nb,corr}$ are the error-corrected annual volume changes.

Appendix D: Area (A) and sediment volume (V) of the sediment filling and the sliding scenarios Sc1-5 of the Sattelkar cirque 07/2022 and 07/2023.

Time	**Description**	**A [m^2]**	**V [m^3]**
07/2022	Sc1	184,385	1,351,800 ± 67,590
	Sc2	165,549	1,093,155 ± 54,658
	Sc3	188,703	1,420,796 ± 71,040
	Sc4	191,683	1,508,309 ± 75,415
	Sc5	223,016	1,892,498 ± 94,625
07/2023	Sc1	184,385	1,197,028 ± 59,851
	Sc2	165,549	954,424 ± 47,721
	Sc3	188,703	1,262,682 ± 63,134
	Sc4	191,683	1,349,312 ± 67,466
	Sc5	223,016	1,707,981 ± 85,399

Appendix E: Error-corrected sediment exhaustion of the scenarios Sc1-5. $V_{corr,nb}$ is the sediment discharge of the landslide based on the extrapolation of the error-corrected trend of 2012-2023, V the remaining sediment volume in the landslide area and $V_{\pm 5\%}$ the remaining volume considering the uncertainty range.

Date	**$V_{corr,nb}$ [m³/a]**	**V**					**V+5%**					**V-5%**				
		Sc1	**Sc2**	**Sc3**	**Sc4**	**Sc5**	**$Sc1_{+5\%}$**	**$Sc2_{+5\%}$**	**$Sc3_{+5\%}$**	**$Sc4_{+5\%}$**	**$Sc5_{+5\%}$**	**$Sc1_{-5\%}$**	**$Sc2_{-5\%}$**	**$Sc3_{-5\%}$**	**$Sc4_{-5\%}$**	**$Sc5_{-5\%}$**
01.01.23	-35,531	1,274,414	1,023,789	1,341,739	1,428,810	1,800,240	1,338,134	1,074,979	1,408,826	1,500,251	1,890,251	1,210,693	972,600	1,274,652	1,357,370	1,710,228
01.01.24	-84,890	1,189,524	938,900	1,256,849	1,343,921	1,715,350	1,253,245	990,089	1,323,936	1,415,361	1,805,362	1,125,803	887,710	1,189,762	1,272,480	1,625,338
01.01.25	-86,328	1,103,196	852,571	1,170,521	1,257,593	1,629,022	1,166,917	903,761	1,237,608	1,329,033	1,719,034	1,039,475	801,382	1,103,434	1,186,152	1,539,010
01.01.26	-87,767	1,015,429	764,805	1,082,754	1,169,826	1,541,255	1,079,150	815,994	1,149,841	1,241,267	1,631,267	951,709	713,615	1,015,667	1,098,386	1,451,243
01.01.27	-89,205	926,224	675,600	993,549	1,080,621	1,452,050	989,945	726,789	1,060,636	1,152,062	1,542,062	862,504	624,410	926,462	1,009,181	1,362,038
01.01.28	-90,643	835,581	584,956	902,906	989,978	1,361,407	899,302	636,146	969,993	1,061,418	1,451,419	771,860	533,767	835,819	918,537	1,271,395
01.01.29	-92,082	743,499	492,875	810,824	897,896	1,269,325	807,220	544,064	877,911	969,336	1,359,337	679,778	441,685	743,737	826,455	1,179,313
01.01.30	-93,520	649,979	399,354	717,304	804,375	1,175,805	713,700	450,544	784,391	875,816	1,265,817	586,258	348,165	650,217	732,935	1,085,793
01.01.31	-94,959	555,020	304,396	622,345	709,417	1,080,846	618,741	355,585	689,432	780,857	1,170,858	491,299	253,206	555,258	637,976	990,834
01.01.32	-96,397	458,623	207,998	525,948	613,020	984,449	522,344	259,188	593,035	684,460	1,074,461	394,902	156,809	458,861	541,579	894,437
01.01.33	-97,836	360,787	110,163	428,112	515,184	886,613	424,508	161,352	495,199	586,624	976,625	297,067	58,973	361,025	443,743	796,601
01.01.34	-99,274	261,513	10,889	328,838	415,910	787,339	325,234	62,078	395,925	487,350	877,351	197,793	0	261,751	344,469	697,327
01.01.35	-100,713	160,801	0	228,126	315,197	686,626	224,521	0	295,212	386,638	776,638	97,080	0	161,039	243,757	596,614
01.01.36	-102,151	58,650	0	125,975	213,046	584,475	122,370	0	193,062	284,487	674,487	0	0	58,888	141,606	494,463
01.01.37	-103,589	0	0	22,385	109,457	480,886	18,781	0	89,472	180,897	570,898	0	0	0	38,016	390,874
01.01.38	-105,028	0	0	0	4,429	375,858	0	0	0	75,870	465,870	0	0	0	0	285,846
01.01.39	-106,466	0	0	0	0	269,392	0	0	0	0	359,404	0	0	0	0	179,380
01.01.40	-107,905	0	0	0	0	161,487	0	0	0	0	251,499	0	0	0	0	71,475
01.01.41	-109,343	0	0	0	0	52,144	0	0	0	0	142,156	0	0	0	0	0
01.01.42	-110,782	0	0	0	0	0	0	0	0	0	31,375	0	0	0	0	0
01.01.43	-112,220	0	0	0	0	0	0	0	0	0	0	0	0	0	0	0

Appendix F: Sediment exhaustion of the scenarios Sc1-5 without error-correction. V_{nb} is the sediment discharge of the landslide based on the extrapolation of the linear, non-corrected trend of 2012-2023, V the remaining sediment volume in the landslide area and V±5% the remaining volume considering the uncertainty range.

Date	**$V_{corr,nd}$ [m^3/a]**	**V**					**$V_{+5\%}$**					**$V_{-5\%}$**				
		Sc1	**Sc2**	**Sc3**	**Sc4**	**Sc5**	**Sc1$_{+5\%}$**	**Sc2$_{+5\%}$**	**Sc3$_{+5\%}$**	**Sc4$_{+5\%}$**	**Sc5$_{+5\%}$**	**Sc1$_{-5\%}$**	**Sc2$_{-5\%}$**	**Sc3$_{-5\%}$**	**Sc4$_{-5\%}$**	**Sc5$_{-5\%}$**
01.01.23	-35,531	1,274,414	1,023,789	1,341,739	1,428,810	1,800,240	1,338,134	1,074,979	1,408,826	1,500,251	1,890,251	1,210,693	972,600	1,274,652	1,357,370	1,710,228
01.01.24	-100,691	1,173,723	923,098	1,241,048	1,328,119	1,699,549	1,237,443	974,288	1,308,135	1,399,560	1,789,560	1,110,002	871,909	1,173,961	1,256,679	1,609,537
01.01.25	-105,347	1,068,376	817,751	1,135,701	1,222,772	1,594,202	1,132,096	868,941	1,202,788	1,294,213	1,684,213	1,004,655	766,562	1,068,614	1,151,332	1,504,190
01.01.26	-110,003	958,373	707,748	1,025,698	1,112,769	1,484,199	1,022,093	758,938	1,092,785	1,184,210	1,574,210	894,652	656,559	958,611	1,041,329	1,394,187
01.01.27	-114,659	843,714	593,089	911,039	998,110	1,369,540	907,434	644,279	978,126	1,069,551	1,459,551	779,993	541,900	843,952	926,670	1,279,528
01.01.28	-119,315	724,399	473,774	791,724	878,795	1,250,225	788,119	524,964	858,811	950,236	1,340,236	660,678	422,585	724,637	807,355	1,160,213
01.01.29	-123,971	600,428	349,803	667,753	754,824	1,126,254	664,148	400,993	734,840	826,265	1,216,265	536,707	298,614	600,666	683,384	1,036,242
01.01.30	-128,627	471,801	221,176	539,126	626,197	997,627	535,521	272,366	606,213	697,638	1,087,638	408,080	169,987	472,039	554,757	907,615
01.01.31	-133,283	338,518	87,893	405,843	492,914	864,344	402,238	139,083	472,930	564,355	954,355	274,797	36,704	338,756	421,474	774,332
01.01.32	-137,939	200,579	0	267,904	354,975	726,405	264,299	1,144	334,991	426,416	816,416	136,858	0	200,817	283,535	636,393
01.01.33	-142,595	57,984	0	125,309	212,380	583,810	121,704	0	192,396	283,821	673,821	0	0	58,222	140,940	493,798
01.01.34	-147,251	0	0	0	65,129	436,559	0	0	45,145	136,570	526,570	0	0	0	0	346,547
01.01.35	-151,907	0	0	0	0	284,652	0	0	0	0	374,663	0	0	0	0	194,640
01.01.36	-156,563	0	0	0	0	128,089	0	0	0	0	218,100	0	0	0	0	38,077
01.01.37	-161,219	0	0	0	0	0	0	0	0	0	56,881	0	0	0	0	0
01.01.38	-165,875	0	0	0	0	0	0	0	0	0	0	0	0	0	0	0